

## Numerical simulation of turbulent, oscillatory flow over sand ripples

Brian C. Barr and Donald N. Slinn

Department of Civil and Coastal Engineering, University of Florida, Gainesville, Florida, USA

Thomas Pierro

Department of Ocean Engineering, Florida Atlantic University, Boca Raton, Florida, USA

Kraig B. Winters

Scripps Institution of Oceanography, University of California, San Diego, La Jolla, California, USA

Received 11 November 2002; revised 7 June 2004; accepted 22 June 2004; published 21 September 2004.

[1] Turbulent oscillatory flow over sand ripples is examined using three-dimensional numerical simulations. The model solves the time-dependent Navier-Stokes equations on a curvilinear grid in a horizontally periodic domain. The flow transitions to turbulence and the presence of sand ripples increases the rate of dissipation of shoaling wave energy compared to flow over a smooth boundary. The influence of the ripple shape is shown to alter the mean flow field and affect the induced drag and dissipation rates. Shear instabilities near the boundary during phases of flow reversal resulting in vortex shedding from the ripple crest produce a continuously turbulent boundary layer, differing from results obtained in simulations over smooth boundaries. *INDEX TERMS:* 4546 Oceanography: Physical: Nearshore processes; 4558 Oceanography: Physical: Sediment transport; 4568 Oceanography: Physical: Turbulence, diffusion, and mixing processes; *KEYWORDS:* turbulent boundary layer, drag coefficient, dissipation rate

**Citation:** Barr, B. C., D. N. Slinn, T. Pierro, and K. B. Winters (2004), Numerical simulation of turbulent, oscillatory flow over sand ripples, *J. Geophys. Res.*, 109, C09009, doi:10.1029/2002JC001709.

### 1. Introduction

[2] Fluid stresses on the seabed and turbulent mixing in the wave bottom boundary layer play major roles in the suspension and transport of sediment and contribute significantly to wave energy dissipation. We employ computational fluid dynamics (CFD) to simulate turbulent flows in the wave bottom boundary layer utilizing nonlinear, finite difference solutions to the unsteady, three-dimensional Navier-Stokes equations. The focus of the study is to simulate turbulent flows due to steady and monochromatic wave forcing over sand ripples of various shapes and to compare the results with flows over smooth beds to determine how the flow dynamics and statistics adjust in the presence of rippled topography. We employ natural relationships between ripple dimensions and wave-induced flow parameters to consider how the boundary layer may behave at different stages of ripple formation. The main motivation is to quantify wave energy dissipation rates and to develop an improved understanding of oscillatory flow over sand ripples.

[3] The wave bottom boundary layer (WBBL) refers to the thin area of fluid that lies closest to the seabed. On a broad shelf it can dissipate significant energy from shoaling surface waves [Mei, 1989]. Throughout most of the water column, oceanic hydrodynamics may be reasonably well described by inviscid, irrotational fluid theory. These assumptions, however, do not hold within

the bottom boundary layer. Here complex nonlinear relationships exist between fluid and sediment in a layer of high vorticity, where the shear stresses associated with turbulence and viscosity are significant. The fluid may burst into turbulence near the seabed due to shear instabilities, dissipating energy from surface waves and large-scale currents, and driving the suspension and transportation of bottom sediments. The motion in the WBBL interacts with the seabed and produces a coupled system. The seafloor provides a sink of wave energy, and the wave field liberates sand particles from the seabed. The particles may become entrained in the water column, reducing water clarity and transporting sediment to new locations, leading to erosion or bed form adjustments. Under conditions of oscillatory flow, sand ripples can be formed locally as a result of particle redistribution and positive feedback in the coupled system. As ripples grow, their presence influences the dynamics of the turbulent boundary layer. As a result of the increase in wall roughness, the net turbulent wave energy dissipation rate may increase. For quasi-stationary wave fields, the coupling between fluid motion and particle redistribution may continue to alter the seabed until a quasi-steady state is achieved and the ripples maintain their shape or migrate slowly. Net effects such as beach erosion, increased bottom drag on mean currents, and wave damping may become more significant as the ripples influence the flow, and the combined effect of surface waves, tides, and currents in the nearshore environment [Voropayev *et al.*, 1999].

[4] Previous researchers investigating waves, currents, and bedforms have found that the flows can present highly nonlinear and complex relationships. Studies as early as that of *Ayrton* [1910] observed connections between ripple evolution and vortex formation at the ripple crests in oscillatory flows. *Grant and Madsen* [1979] presented an empirically based theory to describe the combined motion of oscillatory waves and steady mean currents in the vicinity of a rough bottom. They showed that there is a nonlinear interaction between waves and currents and that even a weak current can be enough to initiate and maintain a net sediment transport. An important prediction of their eddy viscosity model was that the mean current within the boundary layer may be distorted due to the presence of ripples. *Trowbridge and Agrawal* [1995] validated these observations with field measurements of the wave bottom boundary layer using a profiling laser-Doppler velocimeter. They noted that waves and currents over sandy beaches experience an effective bottom roughness associated with the existence of waveformed sand ripples. *Trowbridge and Madsen* [1984] studied oscillatory turbulent flow near a rough seabed from linearized surface waves and made an analogy to steady turbulent flow. The analogy provides the basis for a time-varying eddy viscosity model that was used to obtain approximate closed-form solutions to the one-dimensional boundary layer equations. *Mathisen and Madsen* [1996a, 1996b] also employed an eddy viscosity model to show that a single characteristic roughness may be used to represent pure currents, pure waves, and combined flows over identical topographies. In 1999, they extended their work by introducing spectral waves and showed that the random nature and superposition of these waves has an important effect on eddy formation and energy dissipation [*Mathisen and Madsen*, 1999].

[5] *Ranasoma and Sleath* [1994] conducted laboratory studies of combined oscillatory and steady flow over ripples and noted large-scale momentum exchanges produced by vortex formation associated with rippled topography. *Longuet-Higgins* [1981] studied oscillating flow over steep ripples numerically using the assumption that the sand-water interface in the wave bottom boundary layer is fixed. In this approximation, it was assumed that flow separation takes place at the ripple crests as vortex pairs are convected upward. Field experiments conducted by *Chang and Hanes* [2004] and *Hanes et al.* [2001] utilized acoustic instrumentation to measure the suspended sediment concentration over low-amplitude wave orbital ripples. The ripples possessed a low steepness and exhibited well-rounded crests compared to classic vortex ripples. Their studies indicated significant horizontal advection of clouds of suspended sediment entrained in the boundary layer by the wave-induced orbital fluid motion. Other investigations in sand ripple dynamics were made by *Voropayev et al.* [1999], who showed that the bed shape may not ever reach a true steady state and that time instabilities allow for slow variations in ripple position and subsequent migration. *Trouw et al.* [2000] presented results from a numerical model describing resuspension of sediment compared with data from full-scale laboratory experiments and showed that the standard  $\kappa - \epsilon$  model may underpredict the velocity and shear stress in oscillatory flows above a rippled bed.

[6] Numerical studies of oscillatory flow in connection with wavy surfaces were performed by *Ralph* [1986, 1988] and *Sobey* [1980, 1982, 1983], but mainly focused on internal flows away from a wavy wall. In 1990, *Blondeaux and Vittori* [1991] presented qualitative results of oscillatory flow close to the sea bottom with a two-dimensional numerical approach utilizing spectral methods and finite difference approximations. *Fredsoe et al.* [1999] used the  $\kappa - \omega$  model of *Wilcox* [1988] to simulate waves plus a current over sand ripples and noted that the shape and steepness of the ripple were very important in obtaining a strong separation bubble at the crest. *Scandura et al.* [2000] numerically investigated three-dimensional flow over sand ripples for Reynolds numbers in the range of 100 to 2000. *Calhoun and Street* [2001] used large eddy simulations to investigate neutrally stratified unidirectional steady flow over a wavy bed and found that the area over the center of the trough is highly turbulent. Furthermore, they confirmed the existence of a strong shear layer located in the lee of the ripple crest that weakens considerably with the lowering of the ripple amplitude. Recently, *Moneris and Slinn* [2004] quantified wave energy dissipation in turbulent boundary layers over a flat bed with direct numerical simulations in three dimensions utilizing the model developed by *Slinn and Riley* [1988].

[7] The work presented in this study uses the model developed by *Winters et al.* [2000], to investigate the dynamics of the boundary layer with periodic topographic features and to compare turbulence levels and dissipation rates to those of a smooth seabed.

## 2. Methodology

[8] Our CFD model utilizes the pressure projection method to solve the three-dimensional, unsteady, Navier-Stokes equations for an incompressible, homogeneous fluid on curvilinear coordinates [*Winters et al.*, 2000]. The model employs a third-order Adams-Bashforth variable time stepping procedure that reduces the time step to maintain the stability of the model in phases of particularly strong or turbulent flows and increases the time step smoothly when the flow is less energetic to maximize computational efficiency. Other model features include fourth-order compact spatial differences and filters for dealiasing [*Lele*, 1992], the fourth-order multigrid method to solve for the pressure field (MudPack [*Adams*, 1991]), the option of using the Smagorinski subgrid closure [*Deardorff and Willis*, 1967] for large eddy simulations (LES), and the capability to simulate complex bottom topographies.

[9] Figure 1 sketches the problem geometry and computational domain. Here  $\eta$  is the wave amplitude,  $\lambda$  is the wavelength, and  $h$  is the water depth. Since we are concerned with the flows that arise in the wave bottom boundary layer over periodic ripples, a small periodic domain of approximately  $250 \text{ cm}^3$  is simulated. The bottom boundary is a fixed rigid wall satisfying the “no-slip” boundary condition, while the top boundary is a fixed rigid lid implementing “free-slip” conditions. The four side boundaries of the domain are periodic in order to simulate the flow conditions over a series of ripples in the direction of the flow and to allow three-dimensional flow features to develop in the direction normal to the mean flow.

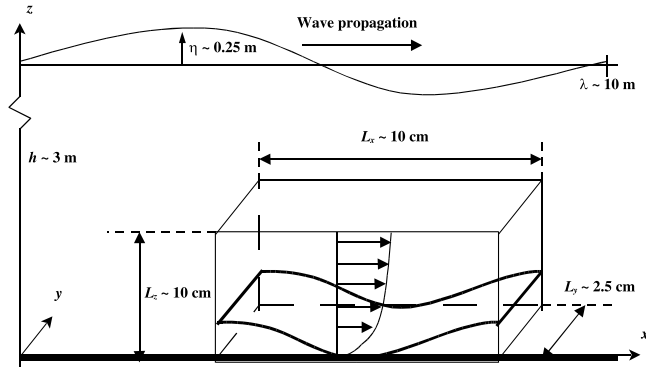


**Figure 1.** Sketch of the problem geometry with a horizontally periodic domain and a sinusoidal bottom boundary under a progressive gravity wave. Note that  $L_x \ll \lambda$ , not shown to scale.

[10] The flow is forced with a depth uniform body force in the  $x$ -direction. Five cases use a time-dependent forcing, as would be felt in a small volume of fluid from the pressure gradient caused by a larger-scale passing surface gravity wave. The body force induces an oscillatory free-stream velocity external to the boundary layer of the form  $U = U_m \sin(\omega t)$ , where  $U_m$  is the maximum wave-induced near bed velocity,  $\omega = 2\pi/T$  is the wave frequency, and  $T$  is the wave period. Three cases use a steady unidirectional forcing.

[11] We pursue high-resolution numerical simulations, utilizing grids up to  $129 \times 33 \times 256$  (1.08 million grid points). The grid spacing near the boundary is on the order of 0.2 mm normal to the wall and 0.8 mm along the wall to optimize the balance between resolution and computational efficiency. Hence with a domain size of  $10 \times 2.5 \times 10$  cm, we resolve features of eddies with length scales between about 5 cm and 0.5 mm. Figure 2 shows the grid layout in an  $x$ - $z$  plane with grid clustering for a typical simulation. At this resolution, the compact filter or Smagorinski LES model primarily contributes to the dissipation of turbulent energy on length scales less than about a millimeter. Our comparisons of the net effects on the flow using either method showed little difference, and we focus our presentation primarily on the results of the simulations that used a constant viscosity ( $\nu = 10^{-6}$  m/s<sup>2</sup>) with the fourth-order compact filter. Issues of model validation, domain size and resolution are discussed in Appendix A.

### 2.1. Grid Transformation

[12] Our approach is to compute approximate solutions to the governing equations on a non-uniform curvilinear mesh in physical  $(x, y, z)$  space by transforming the problem to a cubic lattice of regularly spaced grid points in computational  $(\xi, \eta, \zeta)$  or contravariant coordinates. The geometry is fitted to curvilinear coordinates aligned with the topography.

[13] The three-dimensional computational geometry is transformed using

$$x = x(\xi, \zeta), \quad y = y(\eta), \quad z = z(\xi, \zeta). \quad (1)$$

We note that the physical and contravariant variables in the  $y$ - and  $\eta$ -directions differ by only a constant because the topography is uniform in the direction normal to wave

propagation. To reduce the complexity, the model requires that the coordinate system be orthogonal, satisfying

$$x_\xi z_\zeta + x_\zeta z_\xi = 0. \quad (2)$$

A function may be differentiated with respect to either set of coordinates. In general,

$$\begin{bmatrix} f_\xi \\ f_\zeta \end{bmatrix} = \begin{bmatrix} x_\xi & z_\xi \\ x_\zeta & z_\zeta \end{bmatrix} \begin{bmatrix} f_x \\ f_z \end{bmatrix} \quad (3)$$

$$\begin{bmatrix} f_x \\ f_z \end{bmatrix} = \frac{1}{|J|} \begin{bmatrix} z_\zeta & -z_\xi \\ -x_\zeta & x_\xi \end{bmatrix} \begin{bmatrix} f_\xi \\ f_\zeta \end{bmatrix}, \quad (4)$$

where  $|J| = x_\xi z_\zeta - x_\zeta z_\xi$  is the Jacobian determinant of the transformation.

### 2.2. Governing Equations

[14] The equations of motion for a horizontally forced, three-dimensional, unsteady, incompressible, constant density flow are

$$\frac{\partial u}{\partial t} + \vec{u} \cdot \nabla u = -\frac{1}{\rho} \frac{\partial p}{\partial x} + \nu \nabla^2 u + F^{(x)}, \quad (5)$$

$$\frac{\partial v}{\partial t} + \vec{u} \cdot \nabla v = -\frac{1}{\rho} \frac{\partial p}{\partial y} + \nu \nabla^2 v, \quad (6)$$

$$\frac{\partial w}{\partial t} + \vec{u} \cdot \nabla w = -\frac{1}{\rho} \frac{\partial p}{\partial z} + \nu \nabla^2 w, \quad (7)$$

$$\nabla \cdot \vec{u} = 0, \quad (8)$$

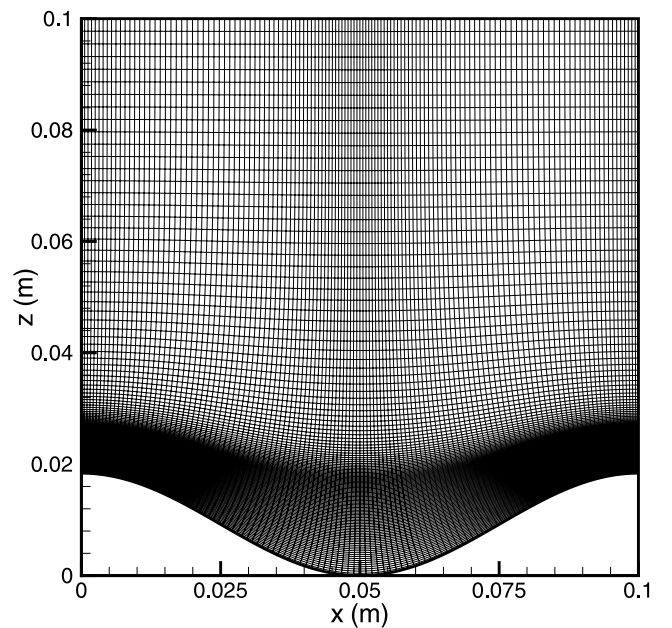


**Figure 2.** Grid layout in the  $x$ - $z$  plane for a sinusoidal ripple 1.8 cm high and 10 cm long.

where the fluid velocities  $u$ ,  $v$ , and  $w$  and pressure  $p$  are the unknowns. The Cartesian coordinates  $(x, y, z)$ , as shown in Figure 1, are respectively oriented shoreward, alongshore, and vertically upward from the bottom boundary respectively;  $t$  is time,  $g$  is the gravitational acceleration,  $\rho$  is a constant fluid density,  $\nu$  is the kinematic viscosity, and  $F^{(x)}$  is the horizontal body force. The Navier-Stokes equations (5)–(8), for the physical variables on a Cartesian grid  $(u, v, w, p)$  are mapped to the contravariant variables on a curvilinear grid  $(U, V, W, P)$  with the differentiation formulas (3) and (4) and the following relations:

$$\begin{bmatrix} u \\ w \end{bmatrix} = \begin{bmatrix} x_\xi & x_\zeta \\ z_\xi & z_\zeta \end{bmatrix} \begin{bmatrix} U \\ W \end{bmatrix}, \quad (9)$$

$$\begin{bmatrix} U \\ W \end{bmatrix} = \frac{1}{|J|} \begin{bmatrix} z_\zeta & -x_\zeta \\ -z_\xi & x_\xi \end{bmatrix} \begin{bmatrix} u \\ w \end{bmatrix}. \quad (10)$$

From here, the derivatives are formed as

$$\frac{\partial u}{\partial \xi} = \frac{\partial u}{\partial x} \frac{\partial x}{\partial \xi} + \frac{\partial u}{\partial z} \frac{\partial z}{\partial \xi} \quad (11)$$

$$\frac{\partial u}{\partial \zeta} = \frac{\partial u}{\partial x} \frac{\partial x}{\partial \zeta} + \frac{\partial u}{\partial z} \frac{\partial z}{\partial \zeta}. \quad (12)$$

The contravariant velocity components  $(U, V, W)$  are oriented along the  $(\xi, \eta, \zeta)$  directions, respectively. The transformation allows a simplified implementation of the discretized boundary conditions, but complicates the governing equations considerably. For example, the  $x$ -momentum equation is transformed to computational space  $\xi$ -momentum equation,

$$\begin{aligned} & \frac{\partial U}{\partial t} + U \frac{\partial U}{\partial \xi} + V \frac{\partial U}{\partial \eta} + W \frac{\partial U}{\partial \zeta} + \frac{1}{|J|} (z_\zeta x_{\xi\xi} - x_\zeta z_{\xi\xi}) U^2 \\ & + \frac{2}{|J|} (x_{\xi\zeta} z_\zeta - z_{\xi\zeta} x_\zeta) U W + \frac{1}{|J|} (z_\zeta x_{\zeta\zeta} - x_\zeta z_{\zeta\zeta}) W^2 \\ & = -\frac{1}{\rho} \frac{(x_\zeta^2 + z_\zeta^2)}{|J|^2} \frac{\partial P}{\partial \xi} + F^\xi \\ & + \nu \left\{ z_\zeta \left[ \frac{1}{|J|} (u_{x\xi} z_\zeta - u_{x\zeta} z_\xi + u_{z\zeta} x_\xi - u_{z\xi} z_\zeta) + u_{\eta\eta} \right] \right. \\ & \left. - z_\xi \left[ \frac{1}{|J|} (w_{x\xi} z_\zeta - w_{x\zeta} z_\xi + w_{z\zeta} x_\xi - w_{z\xi} z_\zeta) + w_{\eta\eta} \right] \right\}. \quad (13) \end{aligned}$$

[15] Similarly, the momentum equations in the  $\eta$  and  $\zeta$ -directions are obtained and the flow is forced with a horizontal pressure gradient,  $F^{(x)} = U_m \omega \cos \omega t$  to produce a mean free stream velocity field approximating  $U_\infty = U_m \sin \omega t$ . Upon transformation to the computational domain, the forcing becomes  $F^{(\xi)} = x_\xi U_m \omega \cos t$  and  $F^{(\zeta)} = x_\zeta U_m \omega \cos \omega t$ . The flows are started from rest. For the steady unidirectional flow cases, the flow is ramped up to  $U_m$  over the first  $T/4$  seconds in the same manner as experienced during the initial quarter period of the oscillatory flows and then held constant with  $U_\infty = U_m$ . The transformed momentum equations are inte-

grated forward in time and the computational space solutions are converted back to physical space for analysis.

### 3. Experiments

[16] The main goal of the experimental plan was to examine the dependence of flow response on ripple topography. To achieve this, several preliminary experiments were performed over a range of Reynolds numbers, wave periods, domain sizes, and bottom contours before the final set of experiments was selected. Flow in the wave bottom boundary layer may be characterized by the Reynolds number,  $Re_\omega = A^2 \omega / \nu$ , based on the wave orbital excursion length  $A$ , defined by  $U_m = A \omega$ . To determine a relevant range of Reynolds numbers and flow parameters that are typical in nature, we reviewed previous studies.

[17] There are two common ways of generating sand ripples in the laboratory [Toit and Sleath, 1981]. The first method was used by Ranasoma and Sleath [1994], who studied combined oscillatory and steady flow conditions over sand ripples generated by oscillating a tray of sand in a still water tank. After ripple formation, they sprinkled the bed with a thin layer of cement to stabilize the ripples so they would maintain their shape throughout the experiments. They found that a stroke of 7.8 cm and a period of 2.45 s produced stable regular two-dimensional ripples 10 cm in length with a crest to trough height of 1.84 cm. From these measurements and with the following relationship,

$$U_m = A \omega = \frac{A 2\pi}{T}, \quad (14)$$

it can be determined that the maximum velocity of oscillation  $U_m$  that produced these ripples was approximately 20 cm/s. The second method of ripple formation, fluid oscillations over an initially flat sandy bed in a wave tank, was used by Voropayev *et al.* [1999]. Owing to the sand-water surface instability, they noted that a critical value of 18 cm/s existed for the maximum velocity of oscillation to induce ‘‘rolling grain sediment transport’’ and subsequent ripple formation for their particular grain size. After about 1 hour of 21 cm/s flow oscillating at approximately 2.95 s, regular two-dimensional vortex ripples, quite similar to those seen by Ranasoma and Sleath [1994], existed in a quasi-steady equilibrium state.

[18] By utilizing the natural combination of wave and ripple parameters determined by the Ranasoma and Sleath [1994] experiments, wave-induced oscillations with a period of 2.45 s and maximum flows of 20 cm/s were chosen for our simulations. Using the dispersion relation for gravity waves and the linear solution for the maximum horizontal particle velocity at the seafloor,

$$\omega^2 = gk \tanh kh \quad (15)$$

$$U_m = \frac{H}{2} \frac{gk}{\omega} \frac{1}{\cosh kh}, \quad (16)$$

we can verify scenarios typical of the nearshore environment that would produce our free stream velocity conditions. One such example is listed in Table 1.

**Table 1.** Typical Wave Characteristics Capable of Producing the Oscillatory Forcing Experienced by the Sand Ripples

Characteristic	Value
Wave height	$\eta = 0.54$ m
Wave length	$\lambda = 9.0$ m
Water depth	$h = 2.8$ m
Wave period	$T = 2.45$ s
Maximum flow	$U_m = 20$ cm/s

[19] The Reynolds number for this flow is approximately  $Re_\omega = 15,000$ . In our experiments, the sand-water interface in the wave bottom boundary layer is assumed fixed and the effect of sand in suspension is neglected. We adopted the *Ranasoma and Sleath* [1994] ripple parameters for two-dimensional ripples, 1.84 cm in height and 10 cm in length, and selected eight test cases.

[20] Simulations were conducted over the three different bed topographies shown in Figure 3. The primary intent was to investigate the effects of ripple shape while keeping the ripple amplitude and wavelength constant and using either oscillatory flow or steady unidirectional flow with the same peak velocity. Table 2 lists the ripple shape, forcing, domain size, and grid resolution for the simulations presented in this study. Simulations conducted with dimension  $10 \times 2.5 \times 20$  cm on a higher resolution grid showed that the eddies remained below  $z = 10$  cm and are not presented.

[21] Case 1 was a control case used for comparison. This case simulated an oscillatory boundary layer over a flat bottom and remained laminar throughout the simulation, consistent with results of previous investigators. The grid points were clustered near the wall to resolve the shear layer near the bed.

[22] The bedform of the basic sinusoidal ripple of Cases 2 and 3 is described by

$$z_o(x) = 0.92 + 0.92 \cos(0.2\pi x) \text{ cm}, \quad (17)$$

shown in Figure 2. The Gaussian ripple, used in Cases 4 and 5, is defined by

$$z_o(x) = 1.84 \exp(-9x^2) \text{ cm}, \quad (18)$$

which has the same amplitude and wavelength as the sine ripple, yet is steeper approaching the crest.

[23] Cases 6 and 7 use a steeper ripple shape, created to approximate a more naturally occurring peaked sand ripple. It is formed from a series of cosine functions of varying amplitudes and frequencies,

$$z_o(x) = 0.5 + 0.7 \sum_{i=1}^5 \frac{\cos(0.2\pi i x)}{2^{i-1}} \text{ cm}. \quad (19)$$

[24] It was found in preliminary tests that the shape of the ripple and grid resolution near the peak were very important in adjusting and capturing the dynamics of the flow, as turbulent eddies were shed from the boundary and convected up into the water column. Case 8 repeated the parameters of Case 2 with the Smagorinski LES subgrid model implemented.

[25] We note that at the present grid resolution, and using these combinations of mathematical techniques, we constructed sand ripples about as steep as possible to still obtain flow simulations that we deemed reliable. Also, we note that each simulation takes on the order of 20 days of CPU time on the current generation of computers at these resolutions when run on a single processor. Increased turnaround times were achieved in some cases by running on parallel computers.

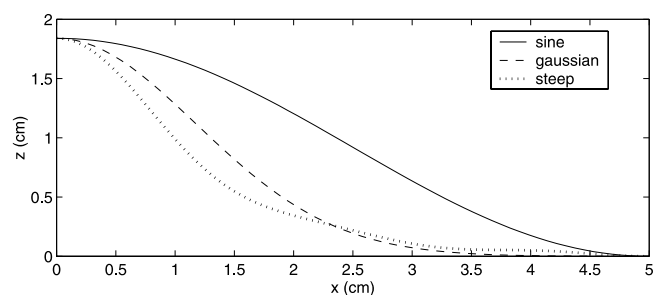
## 4. Results

### 4.1. Velocity Vectors

[26] Samples of velocity vectors at times of maximum flow and flow reversal for oscillatory flow over a sinusoidal ripple are presented in Figure 4. For clarity, the vectors are not shown at all grid points in the  $x$ -direction and the reference vectors are adjusted at the top of every panel to represent the size of a 20 cm/s vector in each frame.

[27] The evidence of three-dimensional effects is most obvious in the top two panels of Figure 4. The first two frames provide plan views ( $x$ - $y$  plane) of velocity vectors on a  $\sigma$ -surface approximately 1 cm from the wall at (Figure 4a) maximum onshore flow and (Figure 4b) flow reversal. During maximum flow, occurrences of cross-shore streaks and variability in the  $y$ -direction can be found throughout the domain. Even though the  $y$ -dimension of the domain is relatively narrow compared to the other dimensions, complete small-scale eddies in the  $x$ - $y$  plane linked to structures noted in the  $x$ - $z$  plane are observed near the ripple crests during flow reversal. The absence of these sorts of three-dimensional features in similar flows over smooth beds (Case 1) indicates that the complexity of the boundary layer is enhanced by the existence of ripples under the forcing of a simple monochromatic wave field at moderate Reynolds number.

[28] Figures 4c and 4d depict a cross section of the domain for oscillatory flow over sinusoidal sand ripples. Again, during times of maximum flow, multidirectional variability is noted in the bottom half of the domain in Figure 4c, while potential flow is maintained at the free-slip upper surface, where  $\partial u/\partial z = 0$ . Figure 4d shows the turnaround at  $t = 15.92$  s. Turbulence due to shear or centrifugal (as seen in the theoretical work of *Hara and Mei* [1990]) instabilities is observed along the slopes of the ripples and particularly near the crest where eddies are shed from the bottom boundary.

**Figure 3.** Profiles of the three ripple shapes used in the simulations.

**Table 2.** Summary of the Cases Presented

Case	Ripple	Forcing	L × W × H, cm	(nx, ny, nz)
1	flat plate	osc	10 × 2.5 × 5	129 × 33 × 65
2	sine	osc	10 × 2.5 × 10	129 × 33 × 129
3	sine	steady	10 × 2.5 × 10	129 × 33 × 129
4	Gaussian	osc	10 × 2.5 × 10	129 × 33 × 129
5	Gaussian	steady	10 × 2.5 × 10	129 × 33 × 129
6	steep	osc	10 × 2.5 × 10	129 × 33 × 129
7	steep	steady	10 × 2.5 × 10	129 × 33 × 129
8	sine	osc	10 × 2.5 × 10	129 × 33 × 129
8	sine	osc	10 × 5.0 × 10	129 × 65 × 129

[29] We note that since the total water depth is larger over the trough than the crest, the mean velocity is slightly less in these regions, a consequence of our rigid free-slip upper boundary and finite domain effects. Simulations with  $L_z = 20$  cm were not significantly different quantitatively or qualitatively, so the finite domain effects were considered acceptable.

#### 4.2. Instantaneous Velocity Profiles

[30] Instantaneous velocity profiles at the midpoint in the  $y$ -dimension of the domain ( $L_y/2$ ) for oscillatory flow over sand ripples are shown in Figures 5, 6, and 7. Profiles are shown at four different times during a wave cycle (flow acceleration, maximum onshore flow, flow deceleration, and flow reversal) at the (Figures 5a, 6a, and 7a) ripple crest, (Figures 5b, 6b, and 7b) ripple down-slope, and (Figures 5c, 6c, and 7c) ripple trough. Intercomparison of the velocity profiles is hampered by the fact that they are instantaneous, and not necessarily representative of any statistical quantities calculated from the flows.

[31] It can be observed that the velocity near the bed changes direction at flow reversal before the free-stream velocity above the ripple crest and slope, but not in the trough. This indicates that the strongest flow separation and vortex shedding occur at or near the crest of the ripple. Another typical feature observed in oscillatory boundary layers is the velocity overshoot that occurs near the bed due to the velocity defect  $U(t) - u(z, t)$ , that alternately adds and subtracts from the free stream at different heights during different phases of the wave [Nielsen, 1992]. This characteristic is most distinctly noted on the ripple slope where the flow accelerates to almost twice that of the free stream velocity.

#### 4.3. Vorticity

[32] Slices of the horizontal vorticity component,

$$\omega_y = \frac{\partial u}{\partial z} - \frac{\partial w}{\partial x}, \quad (20)$$

at times of flow acceleration, maximum flow, flow deceleration and flow reversal for oscillatory flow over the sinusoidal ripple, Case 2, are shown in Figure 8. Figure 9 depicts the vorticity field at the same flow phases for the steep ripple, Case 6. Figure 10 shows flow development for Case 3, steady current over a sine ripple. In each figure, two periodic domains are presented adjacent to each other (two ripple wavelengths) to allow clear visualizations of flow dynamics in the vicinity of ripple crests.

[33] Figure 8b depicts maximum flow over a sinusoidal ripple at  $t = 17.76$  s. Here the flow is to the right, and positive values indicate vorticity with sign into the page. A

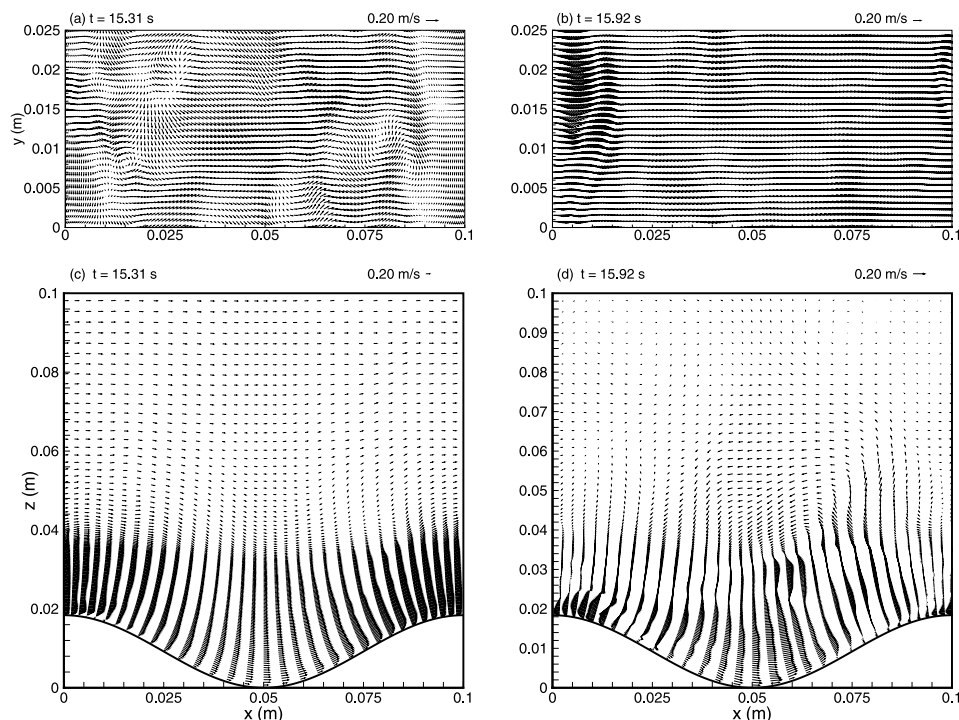


**Figure 4.** Plan views ( $\sigma$ -surfaces) and cross sections of velocity vectors for oscillatory flow over a sinusoidal ripple at phases of maximum onshore flow ( $t = 15.31$  s) and flow reversal ( $t = 15.92$  s).

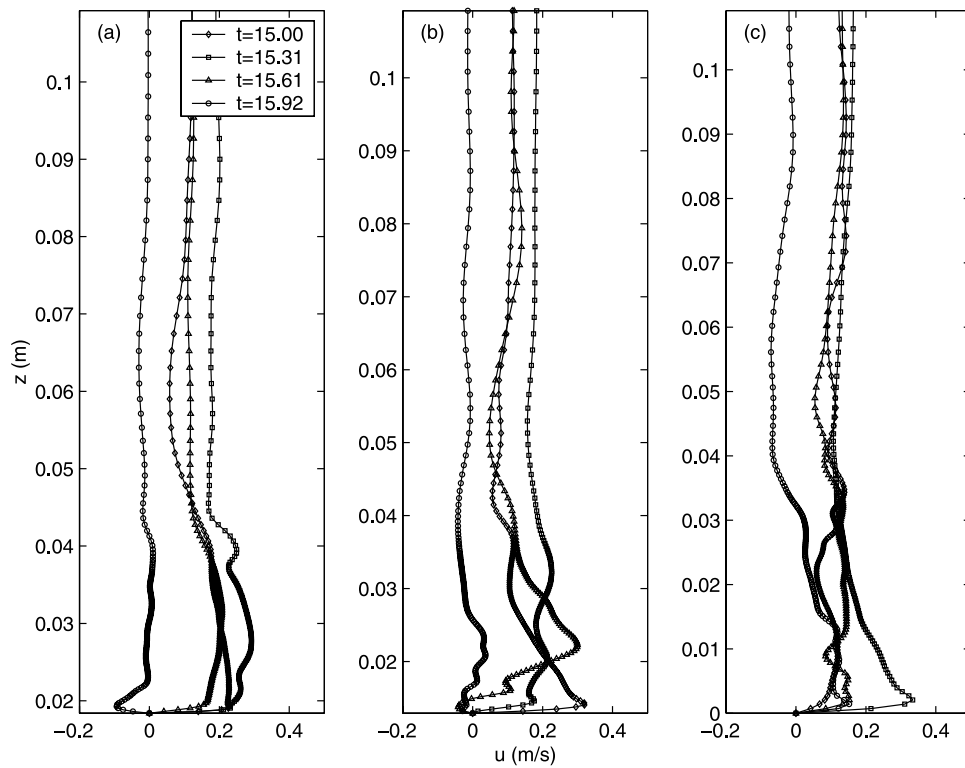


**Figure 5.** Instantaneous velocity profiles over the sinusoidal ripple at  $L_y/2$  for flow acceleration ( $t = 15.00$  s), maximum flow ( $t = 15.31$  s), flow deceleration ( $t = 15.61$  s), and flow reversal ( $t = 15.92$  s) during a wave cycle for locations (a) above the ripple crest, (b) ripple downslope, and (c) ripple trough.

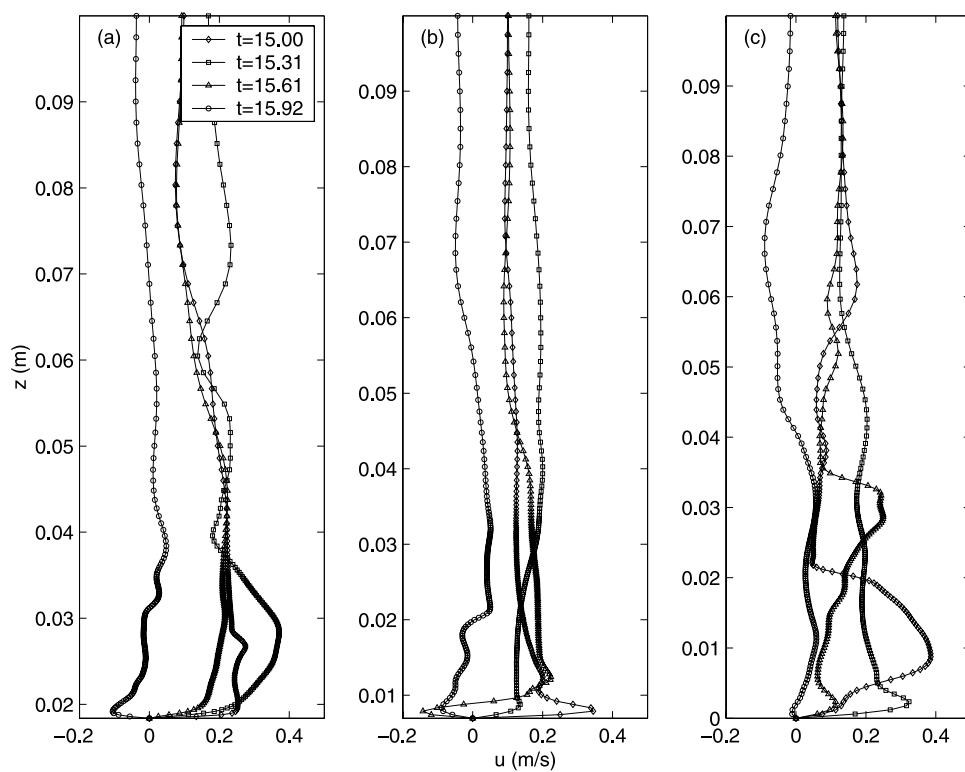


**Figure 6.** Instantaneous velocity profiles over the Gaussian ripple at  $L_y/2$  for flow acceleration ( $t = 15.04$  s), maximum flow ( $t = 15.31$  s), flow deceleration ( $t = 15.61$  s), and flow reversal ( $t = 15.92$  s) during a wave cycle for locations (a) above the ripple crest, (b) ripple downslope, and (c) ripple trough.

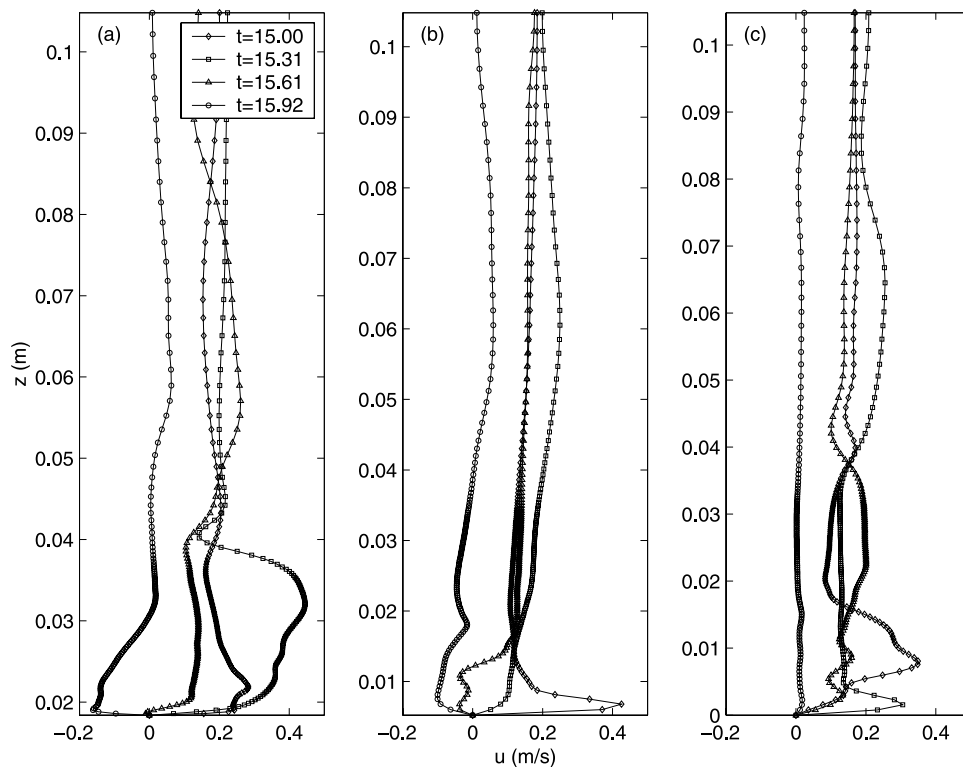


**Figure 7.** Instantaneous velocity profiles over the steep ripple at  $L_y/2$  for flow acceleration ( $t = 15.00$  s), maximum flow ( $t = 15.31$  s), flow deceleration ( $t = 15.61$  s), and flow reversal ( $t = 15.92$  s) during a wave cycle for locations (a) above the ripple crest, (b) ripple downslope, and (c) ripple trough.

strong shear layer is noted along the bottom boundary with vortices being shed in the lee of the ripple crest. Small-scale turbulent eddies can be found propagating up to about 5 cm in the vertical direction of the domain with sustained structures as they pass over the rippled topography. Flow reversal at  $t = 18.36$  s is shown in Figure 8d, and depicts the breakdown of the shear layer as the flow separates from the boundary due to shear instabilities. Rotating structures are observed at the crest of the ripple upon flow reversal similar to results presented by *Blondeaux and Vittori* [1991], using 2-D simulations. They demonstrated that well-organized vortex pairs may be shed from the ripple crest every half cycle. The importance of three-dimensional effects becomes apparent in our results as other small-scale eddies interact with these vortices and produce a variety of structure scales throughout the water column. We note that flow visualizations of these cases can be seen at <http://www.coastal.ufl.edu/~barr/WBBL>.

[34] For comparison, Figure 9 depicts the horizontal vorticity field for flow over the steep ripple at the same phases as the previous figure. It is evident that the near bed shear layer is significantly larger during maximum flow (Figure 9b) and that increasing the steepness of the topography vastly enhances the existence of small-scale turbulence throughout the domain (Figure 9a). Upon flow reversal (Figure 9d), well-defined vortex pairs are shed directly from the ripple crests with much less distortion than observed over sinusoidal ripples, which suggests that ripple shape is important in setting flow patterns in the boundary layer. Three-dimensional effects are evident as turbulent bursts are observed throughout the wave period

and turbulent structures circulate in random directions within the domain.

[35] While sediment transport has not been examined in our numerical experiments, our simulations suggest that the mechanism by which sand ripples maintain their shape is a form of dynamic equilibrium. Sediment may be scoured from the face of the ripple, convected away in suspension by the local velocity, and deposited over the crest and in the lee of the ripples, only to be scoured away again during the next half cycle. We intend to explore this process further, including simulating sediment particles in an extension of the present study.

[36] The last set of vorticity pictures deal with a uniform current in the onshore direction over sinusoidal ripples and are shown in Figure 10. Since there is no wave cycle associated with this case, slices of the horizontal vorticity component are shown for the process of transitioning to turbulence. The major observation from this case is that the flow begins laminar and transitions into a turbulent boundary layer quite rapidly, which grows in thickness over time as turbulent vortices are shed in the lee of the ripple crests until it fills roughly half of the vertical domain. This mechanism of vortex shedding is more apparent in the transitioning flow of Figure 10a, where evolving structures are prevalent in the wake of the ripple. A more extensive investigation of steady flow over sinusoidal topography using similar techniques for a variety of flow speeds and ripple geometries was conducted by *Calhoun and Street* [2001]. The shear layer at the bottom boundary remains quite strong, but becomes detached behind the ripple due to the associated pressure drop and interaction with the turbulent eddies.

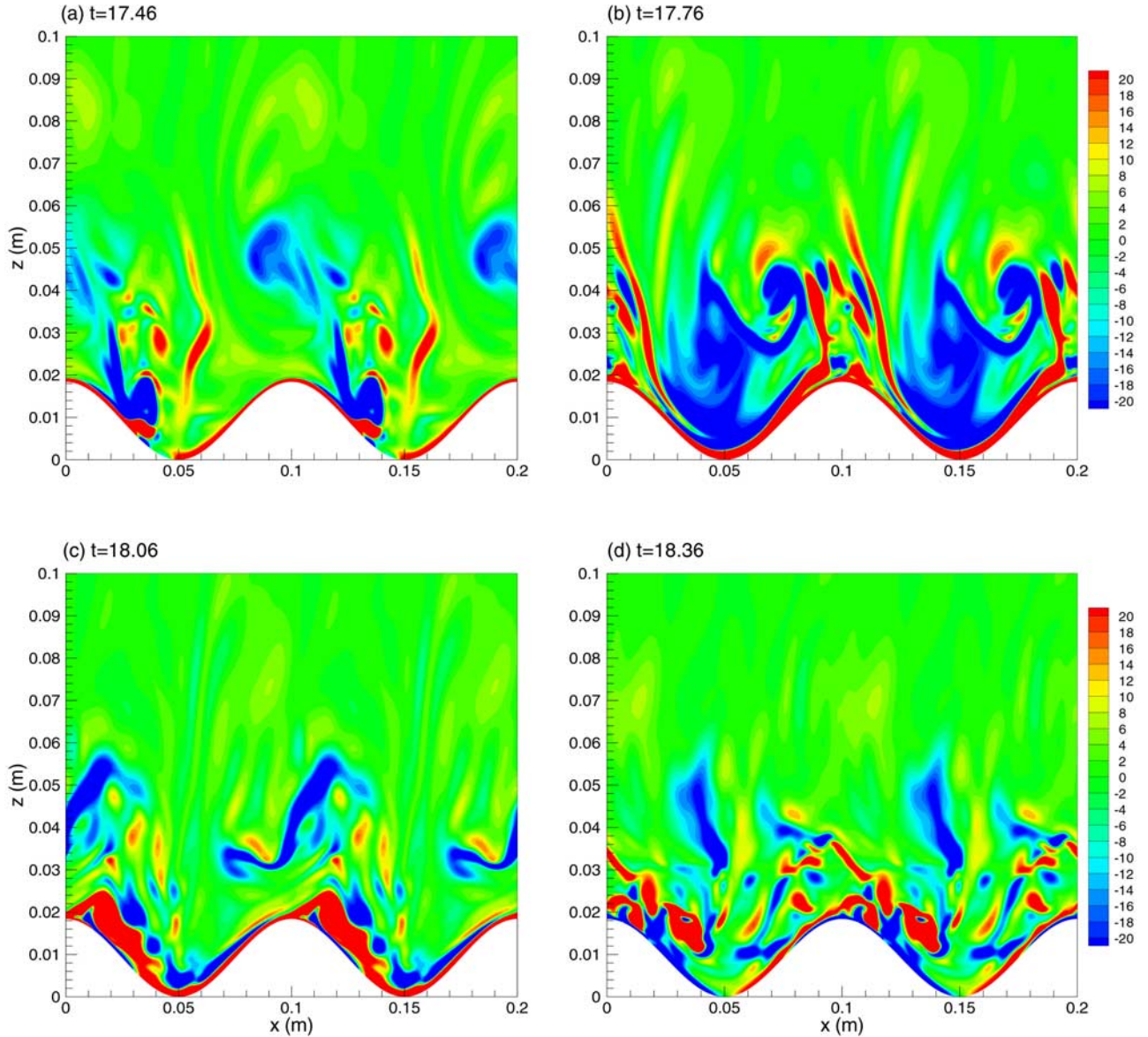


**Figure 8.** Slices of the horizontal vorticity component,  $\omega_y$  ( $\text{s}^{-1}$ ), in an  $x$ - $z$  plane at  $L_y/2$  for a sinusoidal ripple during phases of (a) flow acceleration, (b) maximum onshore flow, (c) flow deceleration, and (d) flow reversal.

[37] We note, for example in Figure 8, that some relatively weak vorticity is present in the region  $5 < z < 10$  cm. We repeated a number of simulations (for five wave periods) using a taller domain extending to  $z = 20$  cm. We found again that the vast majority of the vorticity and turbulence remained restricted to the region below about  $z = 5$  cm and chose to run the smaller domain simulations out longer in time (10 wave periods). We feel that the finite vertical domain effects are tolerable and do not change our main conclusions and observations.

#### 4.4. Turbulent Kinetic Energy

[38] We define the turbulent kinetic energy,

$$\langle TKE \rangle_y(x, z, t) = \langle u'^2 + v'^2 + w'^2 \rangle_y, \quad (21)$$

as the energy of the velocity fluctuations ( $u'$ ,  $v'$ ,  $w'$ ) about the instantaneous mean velocity averaged in the cross-stream direction; that is,  $u = \langle u \rangle_y + u'$  where  $\langle u(x, z, t) \rangle_y$  is averaged in  $y$ .

[39] Time- and volume-averaged values of the turbulent kinetic energy,  $\langle\langle TKE \rangle\rangle$ , as well as typical intensity values during periods of increased turbulence (bursts) are compared for each case in Table 3 over the period ( $4.90 < t < 24.5$  s). It was noted that the 20 cm/s oscillatory flow over a flat bottom (Case 1) remained laminar throughout the simulation and resulting turbulent kinetic energy values were essentially zero. Note also that average RMS velocity fluctuations of approximately 3 cm/s over the bottom half of the domain would give values of  $\langle\langle TKE \rangle\rangle$  of approximately  $1 \times 10^{-3} \text{ m}^2/\text{s}^2$ .

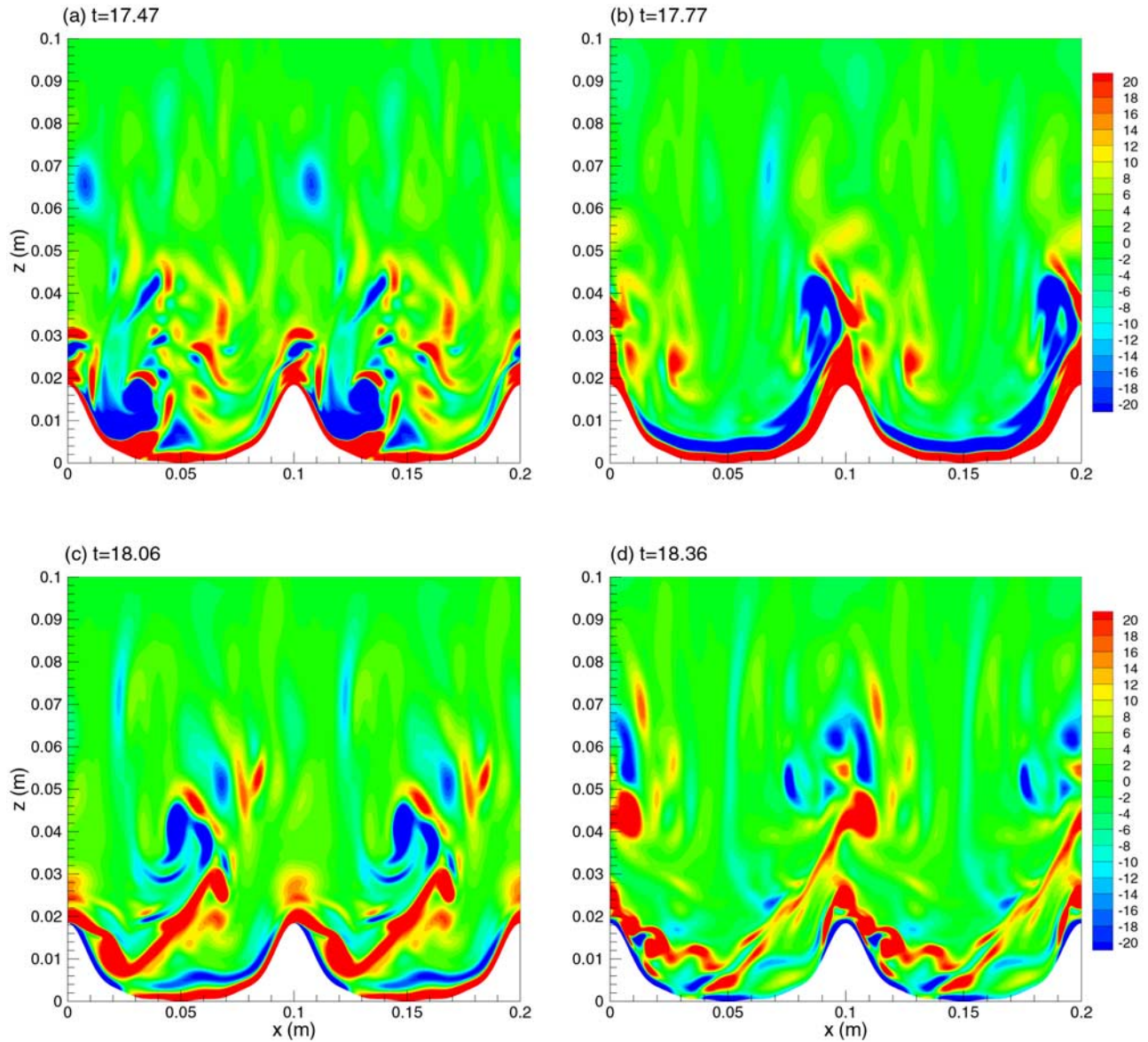


**Figure 9.** Slices of the horizontal vorticity component,  $\omega_y$  ( $\text{s}^{-1}$ ), in an  $x$ - $z$  plane at  $L_y/2$  for a steep ripple during phases of (a) flow acceleration, (b) maximum onshore flow, (c) flow deceleration, and (d) flow reversal.

[40] Time- and spanwise-averaged over the same time period, Figure 11 presents turbulent kinetic energy levels of the oscillatory flows over the three ripple shapes. The main bulk of turbulence is located on either side of the crest, indicating that the flow is relatively well balanced in shedding turbulent vortices from the ripple crests in both directions as the flow turns around every half cycle. Note, however, that there is some asymmetry that may be associated with the initial flow transients. Similar observations were made for uniform flow. As shown in Figure 12, most of the turbulence is concentrated downstream of the ripple crest (since vortices are formed in the lee of the crest and advected downstream). We note that even though the peak velocities are the same,  $U_m = 20$  cm/s, for the oscillatory and unidirectional flows, the RMS total energy in the

system is larger in the steady flow cases, making direct quantitative comparisons imprecise.

[41] Upon increasing the steepness of the ripple, as shown in Figures 11b and 11c, the concentration of turbulence on the flanks of the peak decreases, as it becomes more detached from the crest and distributed fairly uniformly in the trough. Interestingly enough, Table 3 shows the volume-averaged turbulence levels induced by the ripples to be independent of either ripple topography, and only weakly dependent on whether the flow was oscillatory or unidirectional.

[42] For the sinusoidal ripple, the boundary layer becomes thinner over the crest, with a secondary thinning at the trough. However, for the steeper ripples, the boundary layer generally becomes thicker over the crests. The turbulent boundary layer becomes thin again near the base of the

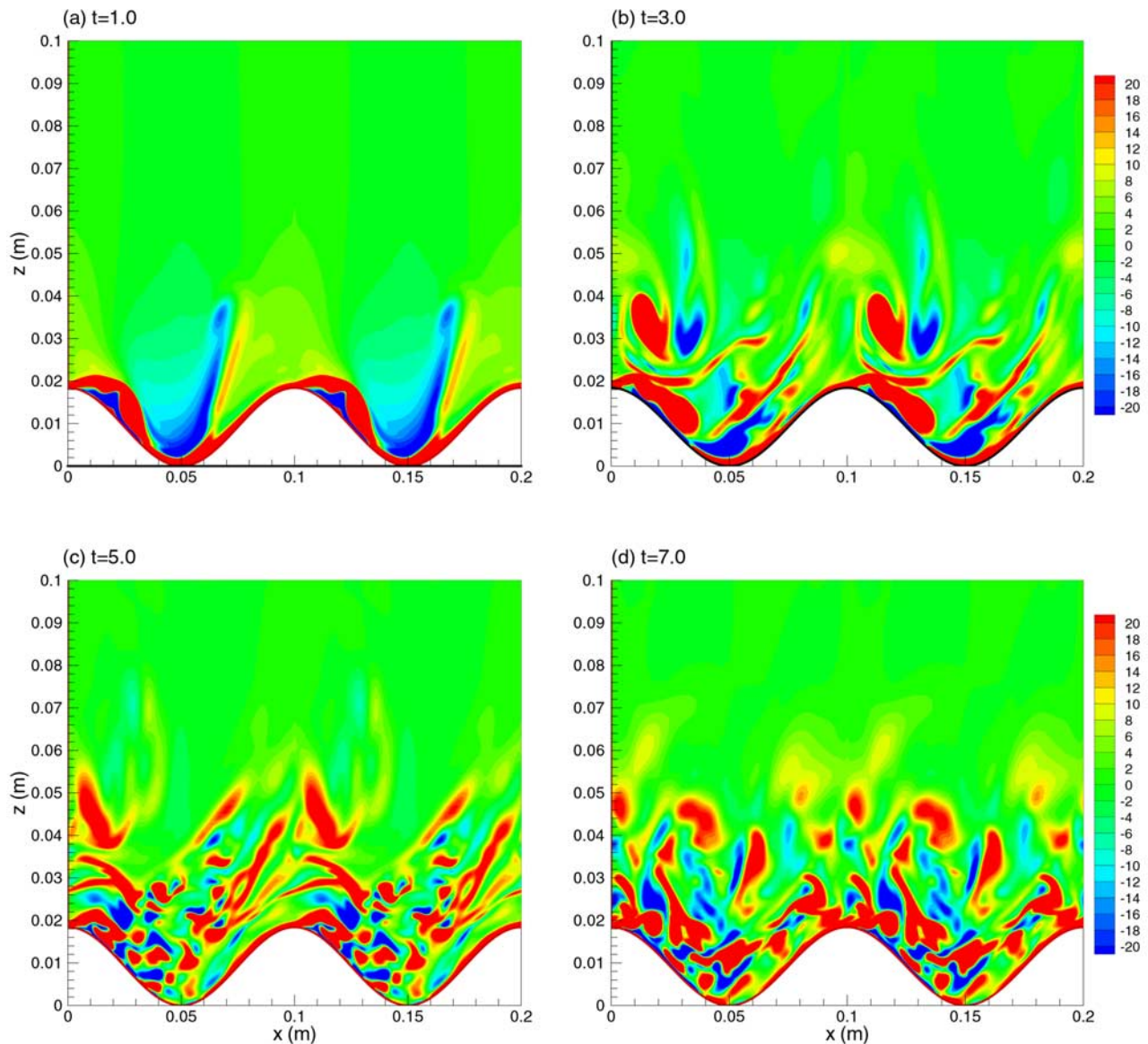


**Figure 10.** Slices of the horizontal vorticity component,  $\omega_y$  ( $\text{s}^{-1}$ ), in an  $x$ - $z$  plane at  $L_y/2$  for a sine ripple during the onset, transition and fully turbulent state.

steeper ripples. There is also a somewhat more pronounced spatial oscillation in the boundary layer thickness for the steady flow, than for the oscillatory flow.

[43] Volume and phase averaged turbulent kinetic energy for the oscillatory cases are shown as a function of phase in Figure 13. Volume and time averaged values for the steady cases are indicated as well. We note that for oscillatory flow over the Gaussian ripple near  $t = 3.0$  s the  $\langle\langle TKE \rangle\rangle$  had a maximum of approximately  $3.5 \times 10^{-3} \text{ m}^2/\text{s}^2$  that was associated with the initial transition from 2-D to 3-D flow that was atypical of turbulence levels achieved by the quasi-steady flow during later wave periods; for this reason the phase averaging was for the eight wave periods for  $4.9 < t < 24.5$ .

[44] For oscillatory flow, the simulations show a double-humped maximum centered around both phases of maximum flow. Ideally, the shape of the curves should be

perfectly symmetrical (the flow should not favor flow in one direction over the other). However, with the limited number of wave periods calculated, and the possibility of transients associated with the initiation process, these phase-averaged values should not be taken as converged statistics. This is especially evident in the oscillatory flow over the sine ripple and less evident for cases with higher turbulence levels.

[45] Results for Case 8, oscillatory flow over the sine ripple using the Smagorinski LES subgrid model, are similar to Case 2 that used a spatially and temporally constant kinematic viscosity ( $\nu = 10^{-6} \text{ m}^2/\text{s}$ ) and the compact filter for submillimeter scales of dissipation. Additional analysis, not shown, indicated that the general flow behavior and integral properties, such as the boundary layer thickness, were similar, independent of the subgrid-scale model. Because we used a clustered grid at the bottom

**Table 3.** Time-Averaged and Typical Peak Levels of Volume-Averaged Turbulent Kinetic Energy,  $\text{m}^2/\text{s}^2$ 

Case	$\langle\langle TKE \rangle\rangle$	Typical Burst
1	$1.27 \times 10^{-13}$	$1.56 \times 10^{-13}$
2	$6.64 \times 10^{-4}$	$1.0 \times 10^{-3}$
3	$8.41 \times 10^{-4}$	$9.7 \times 10^{-4}$
4	$6.84 \times 10^{-4}$	$1.2 \times 10^{-3}$
5	$7.64 \times 10^{-4}$	$1.0 \times 10^{-3}$
6	$6.38 \times 10^{-4}$	$9.4 \times 10^{-4}$
7	$5.89 \times 10^{-4}$	$7.8 \times 10^{-4}$

boundary, we found that we were able to resolve nearly all of the flow features in the 1-cm layer closest to the boundary and the effects of the subgrid filter were felt farther up in the water column as the eddies cascaded down to smaller scales on the less refined grid. We therefore preferred the constant viscosity model.

#### 4.5. Kinetic Energy Dissipation

[46] The total kinetic energy dissipation rate in the model is presented as

$$\epsilon = \epsilon_r + \epsilon_f, \quad (22)$$

where  $\epsilon_f$  represents the energy dissipated in the subgrid scales through the fourth-order compact spatial filtering technique and  $\epsilon_r$  is the viscous dissipation due to friction in the resolved scales defined by

$$\epsilon_r = \mu \left[ 2 \left( \frac{\partial u}{\partial x} \right)^2 + 2 \left( \frac{\partial v}{\partial y} \right)^2 + 2 \left( \frac{\partial w}{\partial z} \right)^2 + \left( \frac{\partial v}{\partial x} + \frac{\partial u}{\partial y} \right)^2 + \left( \frac{\partial w}{\partial y} + \frac{\partial v}{\partial z} \right)^2 + \left( \frac{\partial u}{\partial z} + \frac{\partial w}{\partial x} \right)^2 \right]. \quad (23)$$

Typical peak values associated with turbulent bursts, or phases of maximum flow, and time- and volume-averaged total kinetic energy dissipation rates are compared for each case in Table 4. The results are obtained by averaging over eight wave periods ( $4.90 < t < 24.5$ ) as was done with the turbulent kinetic energy.

[47] Contours of the total energy dissipation rate averaged horizontally ( $y$ -direction) and in time ( $4.90 < t < 24.5$  s) (not shown) for oscillatory flows showed that for these relatively low Reynolds number flows, the largest energy dissipation occurs immediately adjacent to the bottom boundary due to viscous losses and friction at the no-slip wall over the

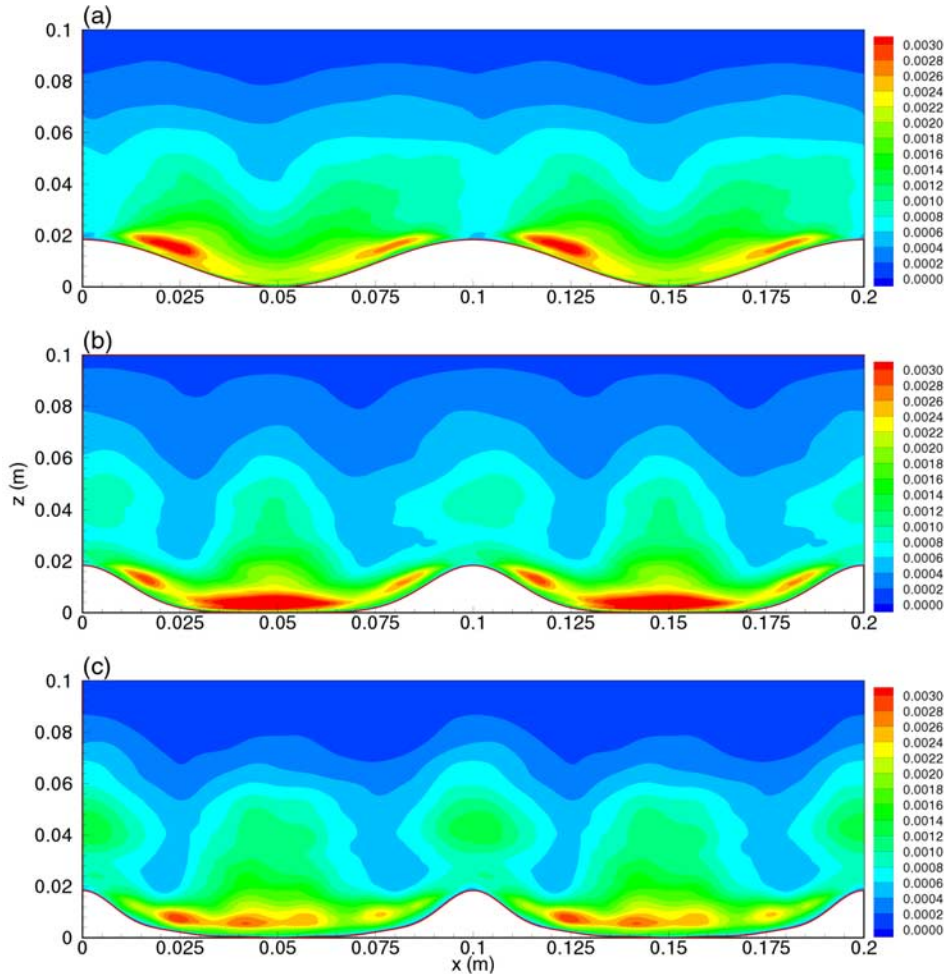


**Figure 11.** Turbulent kinetic energy ( $\text{m}^2/\text{s}^2$ ) averaged both horizontally ( $y$ -direction) and in time for oscillatory flow over (a) sine, (b) Gaussian, and (c) steep ripples.

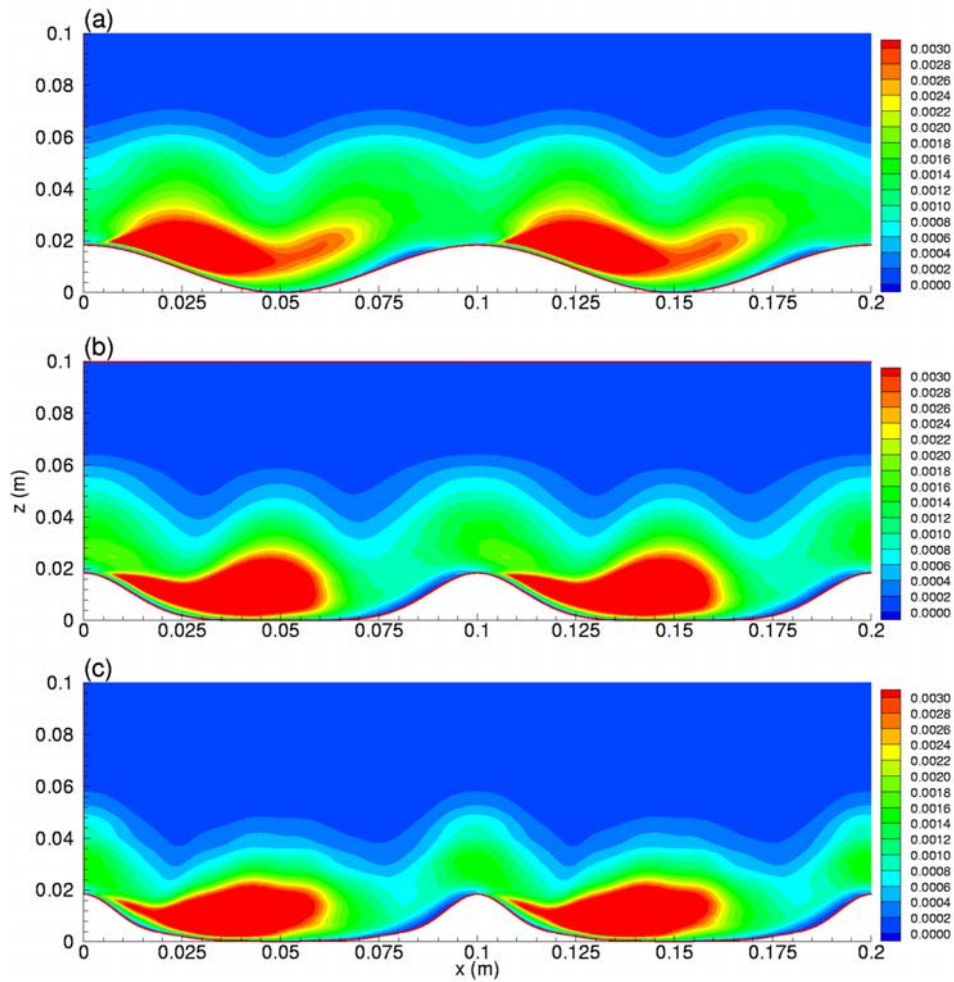


**Figure 12.** Turbulent kinetic energy ( $\text{m}^2/\text{s}^2$ ) averaged both horizontally ( $y$ -direction) and in time for steady flow over (a) sine, (b) Gaussian, and (c) steep ripples.

ripple. Elevated rates of dissipation are also seen in the lee of the ripple within about 1 cm from the wall, corresponding to the higher levels of turbulent kinetic energy found in that region.

[48] Figure 14 depicts the volume and phase-averaged energy dissipation as a function of time for the oscillatory cases. The dissipation function for Case 1 is indicative of oscillatory flows over flat plates, yielding a smooth and periodic response to the laminar flow. For all cases over ripples, the flow becomes turbulent, with a large burst of energy dissipation occurring just after one wave period.

[49] Peak dissipation rates are more than 3 times larger over the ripples compared to the flat plate. Total dissipation rates are higher during phases of strong onshore or offshore flow, in phase with the turbulent kinetic energy. While the average dissipation rates are comparable between the oscillatory and steady flows, the peak rates are higher for oscillatory flows, a somewhat counterintuitive result since the steady flows always have the same amount of mean flow energy as the oscillatory flows do at their maxima. Since dissipation rates and enstrophy are closely related [Pope, 2000], the explanation may be related to the periodic reattachment of the flow to the wall during flow reversal episodes that could produce increased fluxes of vorticity of

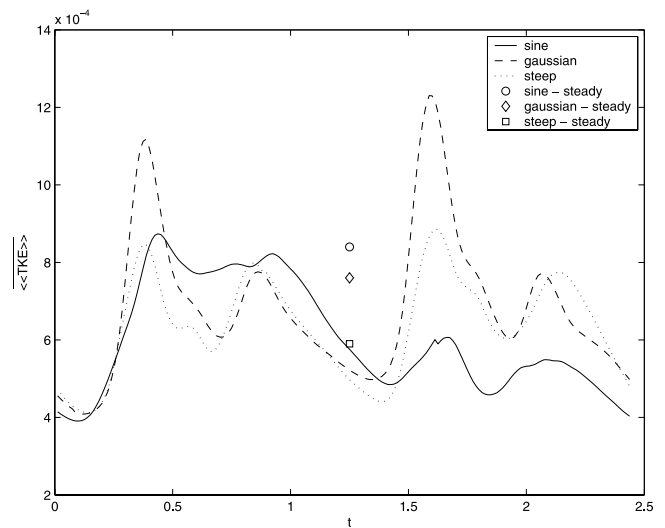


**Figure 13.** Volume- and phase-averaged turbulent kinetic energy  $\langle\langle TKE \rangle\rangle$  ( $\text{m}^2/\text{s}^2$ ) for oscillatory flows. Volume- and time-averaged values for steady flows are also indicated.

**Table 4.** Time-Averaged and Typical Peak Levels of Volume-Averaged Kinetic Energy Dissipation Rates,  $W/m^3$ 

Case	Time Average	Typical Peak
1	0.502	0.84
2	1.815	2.82
3	1.790	2.10
4	1.626	3.13
5	1.535	2.02
6	1.378	2.64
7	0.947	1.39

both signs into the flow in the oscillatory cases. In contrast, the steady flow has a consistent sheltering effect by the ripple crest on the trough that allows a progressive thickening of the viscous sublayer that would lead to a somewhat weaker flux of vorticity into the flow. The net effect could be to allow a higher flux of vorticity and enstrophy into the flow from the wall for the oscillatory cases that could then be dissipated after undergoing the turbulent cascade.

#### 4.6. Shear Stress at the Wall

[50] The wall shear component conventionally defined by

$$\tau_w = \mu \frac{\partial(u \cdot \vec{i} + w \cdot \vec{j})}{\partial n} \quad (24)$$

is evaluated in the physical coordinate system, where  $u$  and  $w$  represent physical space velocities and  $\vec{i}$  is the unit tangential vector to the surface. In Figure 15, the shear stress at the wall is shown in an  $x$ - $y$  plane ( $\sigma$ -surface) for oscillatory flow over sinusoidal ripples during (Figure 15a) maximum onshore flow and (Figure 15b) flow reversal. By viewing the wall shear from a plan view, the three-dimensionality of the model is apparent. The high spatial variability is an important feature because the liberation of particles from the seafloor is dependent on  $|\tau_w|$  and is the first step in sediment transport.

[51] In Figure 15a, the highest value of shear stress occurs at or near the ripple crest during the phase of maximum flow. The phase of flow reversal is shown in Figure 15b and depicts a change in sign of the shear near the ripple crest associated with the velocity defect and compares quite well with the velocity profiles shown in Figure 5. Furthermore, there is evidence in the ripple trough that the shear stress is lagging the free-stream velocity, which is commonly observed in oscillatory boundary layers. We note that critical wall shear stresses of approximately 0.1 to 0.5 Pa are typically sufficient to cause incipient motion of sandy material with mean grain size diameters between about 0.05 and 1 mm, respectively [Julien, 1998]. Hence the viscous wall stresses modeled here would be sufficient to instigate sediment suspension.

[52] The RMS average magnitude of the wall shear component for sinusoidal ripples time-averaged over eight wave periods ( $4.9 < t < 24.5$  s) is given in Figure 15c. It is clear that the highest levels of skin friction occur on the slopes of the ripples, indicating an area where drag forces due to shear stress are maximized. As expected, the levels are spread fairly evenly on either slope and are reasonably uniform in the  $y$ -direction. It is suggested that with a longer simulation (allowing for a greater period of time-averaging)

the degree of variability in the alongshore direction would decrease and the maximum levels of shear stress would occur between the crest and the midpoint of the slope (in this case,  $x = 1.75$  and  $8.25$  cm). This area of high stress may play a major role in the development and migration of sand ripples. The asymmetry in stress between the two sides of the ripple is not so apparent in other simulations, and is attributable to secondary circulation caused by the initial transients.

#### 4.7. Pressure Drag

[53] Form drag due to pressure variations over the length of a sand ripple may be measured and quantified by integrating the  $x$ -component of the pressure force on the wall over the area of the bottom boundary. The resulting integrated form drag or “pressure drag” is defined as

$$D_p = \int \int P_w \sin \theta \, dy \, dx, \quad (25)$$

where  $P_w$  is the (gauge) pressure on the wall and  $\theta$  represents the slope of the ripple at the point where the pressure is applied. Hydrostatic contributions are symmetric and have been removed. Pressure contours on the wall are shown for two phases of the flow over a sinusoidal ripple in Figure 16.

[54] Figure 16a depicts the dynamic pressure on the wall ( $P_w$ ) of a sinusoidal ripple during maximum flow where the flow becomes detached in the lee of the ripple crest. Pressure variations on the wall are found just beyond the crest indicating circulation associated with vortex formation in the wake of the ripple. Figure 16b shows that during flow reversal the pressure forces on the wall are similar on the upslope and downslope of the ripple, but in opposite directions. As the pressure force is everywhere normal to the boundary, this was an expected result during phases of minimal flow and is consistent with the conclusion that form drag is an important factor in flows over rippled topographies.

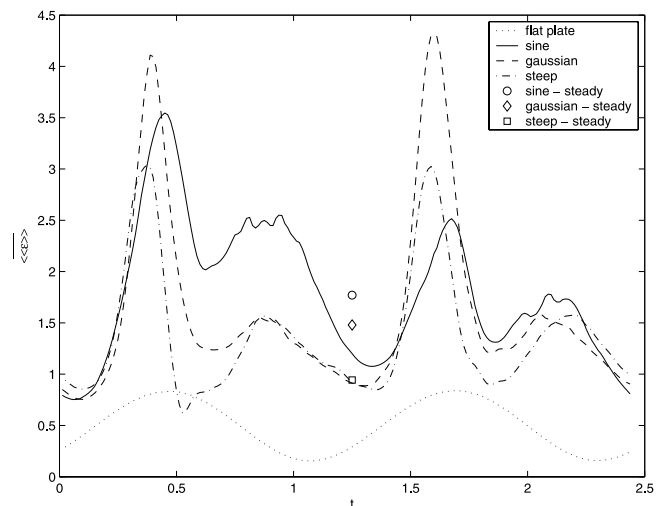


**Figure 14.** Volume- and phase-averaged dissipation rates ( $W/m^3$ ) for oscillatory flow. Volume- and time-averaged values for steady cases are indicated as well.

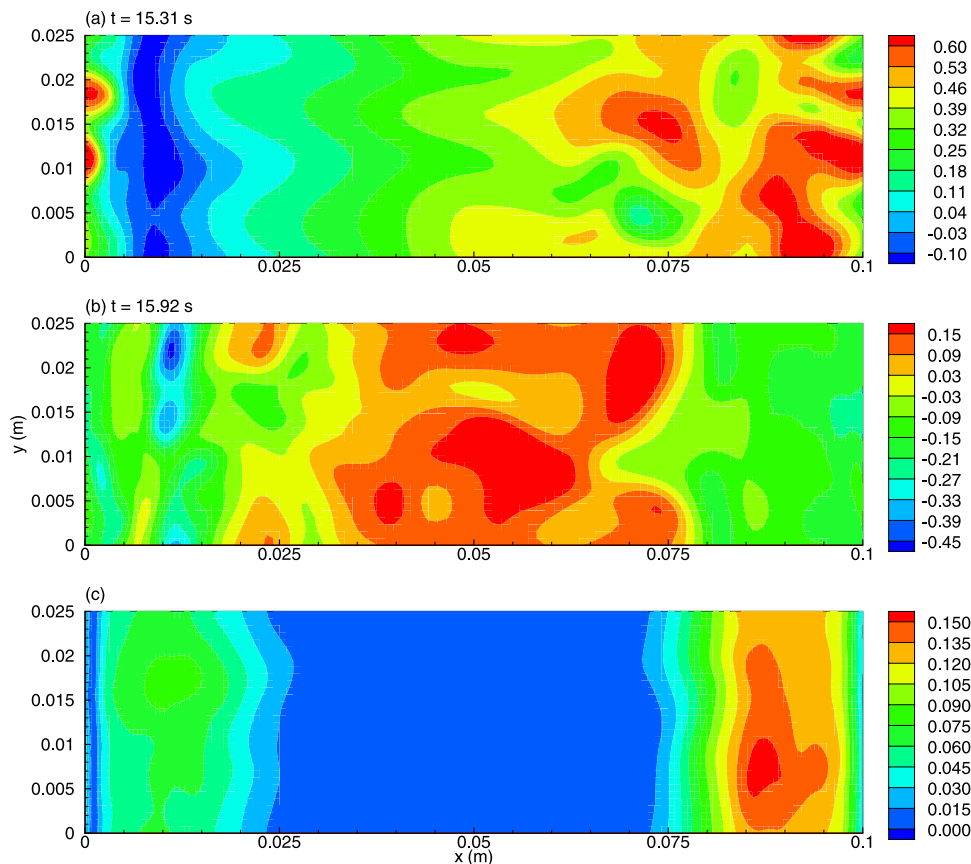


**Figure 15.** Plan views of the wall shear stress (Pa) on the ripple surface for oscillatory flow over a sinusoidal ripple showing (a) maximum flow at  $t = 15.3$  s, (b) flow reversal at  $t = 15.9$  s, and (c) time averaged over eight wave periods ( $4.9 < t < 24.5$ ).

[55] Figure 17 presents a phase averaged comparison of the form drag,  $D_p$ , and viscous drag,  $D_v$ , for the oscillatory cases. As expected, the flat bottom case presents no form drag because the pressure is perpendicular to the flat

boundary and the  $x$ -component is identically zero everywhere. In this case, the drag is purely viscous and we recall the previous result that the flat bottom case maintains the highest average shear stress at the wall because the flow

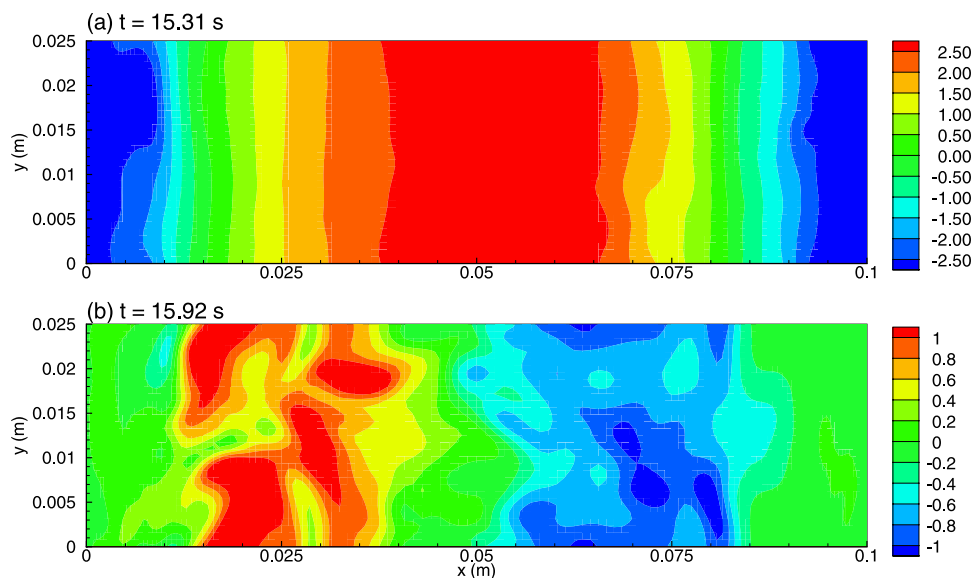


**Figure 16.** Pressure contours (Pa) on the wall for flow over sinusoidal ripples at (a) maximum onshore flow and (b) flow reversal.

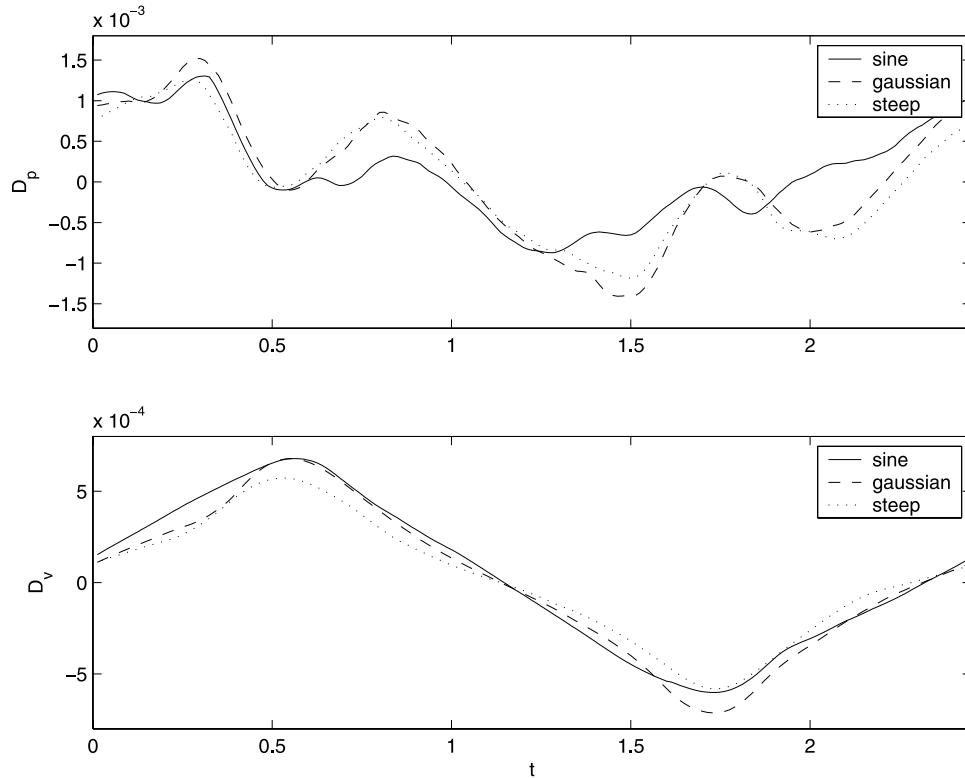


**Figure 17.** Surface and phase-averaged form and viscous drag (N) for the oscillatory cases.

remains attached to the boundary. Table 5 provides a summary of average values of the integrated pressure and viscous drag for each of the seven cases, calculated over the time period  $4.90 < t < 25.0$  s.

[56] With the introduction of ripples, the RMS viscous drag decreases by approximately 25% in the oscillatory cases. The form drag, however, increases.

[57] As the steepness of the ripples increases, the form drag dominates the viscous drag. Even though the viscous drag decreases due to blocking effects and flow separation for steeper ripples, the total drag increases due to the increased pressure force on the variable boundary. We also note that the RMS drag in oscillatory flow exceeds the drag for steady flow for the same peak free stream velocity. As a corollary, the increased flow resistance by the bed forms should cause increased energy dissipation from the shoaling surface waves. Comparison of the total RMS drag from Table 5 with typical peak dissipation rates from Table 4 supports this conclusion.

#### 4.8. Friction Factors

[58] This section treats two applications of potential interest: surface wave attenuation and sediment transport. Wave attenuation will be most affected by the total drag. This can be presented nondimensionally as a coefficient of drag defined as

$$C_D = \frac{2F_D}{\rho U_m^2 A}, \quad (26)$$

where  $F_D$  is the RMS total drag (combined viscous and form drag), and  $A$  is the surface area of the ripple, with values of 25.00, 27.00, 27.80, and 27.96  $\text{cm}^2$ , for the flat plate, sine, Gaussian, and steep ripple, respectively.

[59] For sediment transport, the maximum shear experienced by the ripple will be the driving factor. Similar to the definition of the coefficient of drag, *Jonsson* [1966] defined the dimensionless wave friction factor,

$$f_w = \frac{2\hat{\tau}_w}{\rho U_m^2}, \quad (27)$$

in relation to the maximum shear stress at the wall,  $\hat{\tau}_w$ , and the amplitude of oscillation  $U_m = A\omega$ . He also showed that the friction factor could be adapted to boundary layers developed under uniform currents by replacing  $U_m$  with the steady velocity of the current. *Nielson* [1992] points out that there is a serious shortage of experimental data on boundary layer structure in the turbulent regime. Furthermore, studies made by *Bagnold* [1946], *Carstens et al.* [1969], and *Loftquist* [1986] all used different definitions and terminology when referring to friction factors. Comparing our numerical results to experimental data becomes difficult, even without considering the differ-

**Table 5.** RMS Average of Integrated Viscous ( $D_v$ ), Form ( $D_p$ ), and Total Drag, ( $\text{N} \times 10^{-4}$ )

Case	RMS $D_v$	RMS $D_p$	RMS Total
1	5.18	0.00	5.18
2	4.00	6.45	8.93
3	1.36	5.02	6.16
4	3.99	7.94	10.67
5	1.08	4.86	5.74
6	3.32	7.07	9.27
7	1.00	4.07	4.87

**Table 6.** Maximum Shear ( $\text{N/m}^2$ ), Friction Factors, and Coefficient of Drag for All Cases

Case	Ripple	Forcing	$\hat{\tau}_w$	$f_w$	$C_D$
1	flat	osc	0.293	0.0029	0.0101
2	sine	osc	1.086	0.0106	0.0161
3	sine	steady	0.622	0.0061	0.0111
4	Gaussian	osc	1.020	0.0099	0.0187
5	Gaussian	steady	0.652	0.0063	0.0100
6	steep	osc	1.121	0.0109	0.0161
7	steep	steady	0.716	0.0070	0.0085

ences in bed form shapes. Table 6 presents the results from the simulations. Direct model comparison with field data collected during the SHOWEX experiment are in progress.

## 5. Summary

[60] Numerical investigations of the flow dynamics in the wave bottom boundary layer over sand ripples have been conducted employing a modification of the time-dependent, three-dimensional, fourth-order curvilinear model developed by *Winters et al.* [2000]. At low to moderate Reynolds number, the presence of sand ripples has been observed to induce significantly higher turbulence levels and dissipation rates in the boundary layer compared to flows over a smooth boundary.

[61] The thickness of the wave bottom boundary layer over rippled topography has also been shown to increase, as flows became more complex and unsteady under simple monochromatic forcing. Boundary layer thicknesses have also been shown to be larger for oscillatory flows compared to steady flows over the same topographic features.

[62] For rippled topographies, turbulent bursts originating during flow reversal are not damped out during flow acceleration as they are even at higher Reynolds number (S. Moneris and D. N. Slinn, Numerical simulation of the wave bottom boundary layer over a smooth surface: 1. Three-dimensional simulations, submitted to *Journal of Geophysical Research*, 2004) over flat beds, but remain relatively strong throughout the wave period. The levels of turbulence typically fluctuate over the wave period by about a factor of 2. Separation at the ripple crests has been observed to be a mechanism for the production of turbulence in the boundary layer during phases of maximum flow and has been associated with turbulent boundary layer growth for a uniform current over steep ripples. As the steepness of the ripples increase, the turbulence becomes more focused in the trough and above the ripple crest. For uniform currents over sand ripples, the boundary layer thickness grows slowly in time but does not achieve the same dimension as the oscillatory case during these 25-s simulations.

[63] The simulations suggest that a dynamic equilibrium of scour on the face and deposition in the lee and the increased concentration of turbulent kinetic energy in the lee of the ripple crests could be responsible for redistribution of sediment in suspension to the peaks of the ripples.

[64] The simulations also demonstrate that the average shear stress on the wall decreases with ripple steepness but becomes more localized spatially near the ripple crest with

minima in the troughs. The average wall shear stress is highest for flow over flat beds, suggesting that natural ripples can exist in a state of equilibrium between scour by skin friction and particle settlement due to gravity. The wave friction factor due to shear stress is observed to increase with the presence of ripples. The form drag and consequently the total drag also increase with ripple steepness due to the increasing pressure forces on the variable boundary. Several lines of investigation invite continued work, including comparisons with more complex time series of wave forcing, simulations that include sediment particles, comparison with 1-D WBBL models, and combinations of oscillatory and steady currents in the wave bottom boundary layer.

## Appendix A

### A1. Domain Size

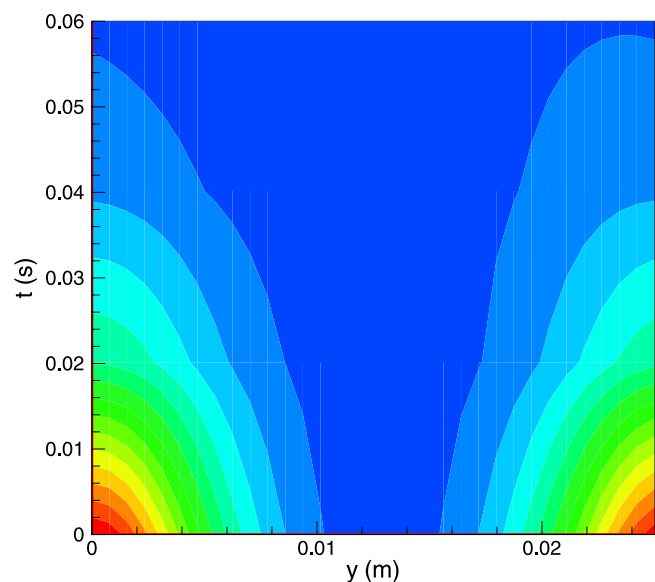
[65] Figure A1 shows the autocorrelation in time and space along the span-wise direction at the ripple crest for the  $v$ -velocity. This indicates that the width of the domain is adequate to capture any instabilities inherent in the flow. Note that this is in contrast to the low Reynolds number numerical studies of *Scandura et al.* [2000], which required a domain width 2.5 times the ripple wavelength. The higher turbulence levels here lead to shorter correlation lengths.

### A2. Grid Resolution

[66] Spectra of the velocities in computational space are presented in Figure A2. While not directly comparable to physical space spectra, it is necessary for the solution to be well resolved in computational space. It is evident that there is little “energy” contained in the highest wave numbers; in the  $\xi$ -direction,  $k_{\max} = 1/64$ .

### A3. Model Validation

[67] In addition to the extensive model validation (detailing the accuracy of scalar diffusion, time-dependent Couette

**Figure A1.** Autocorrelations for the  $v$ -velocity at the ripple crest.

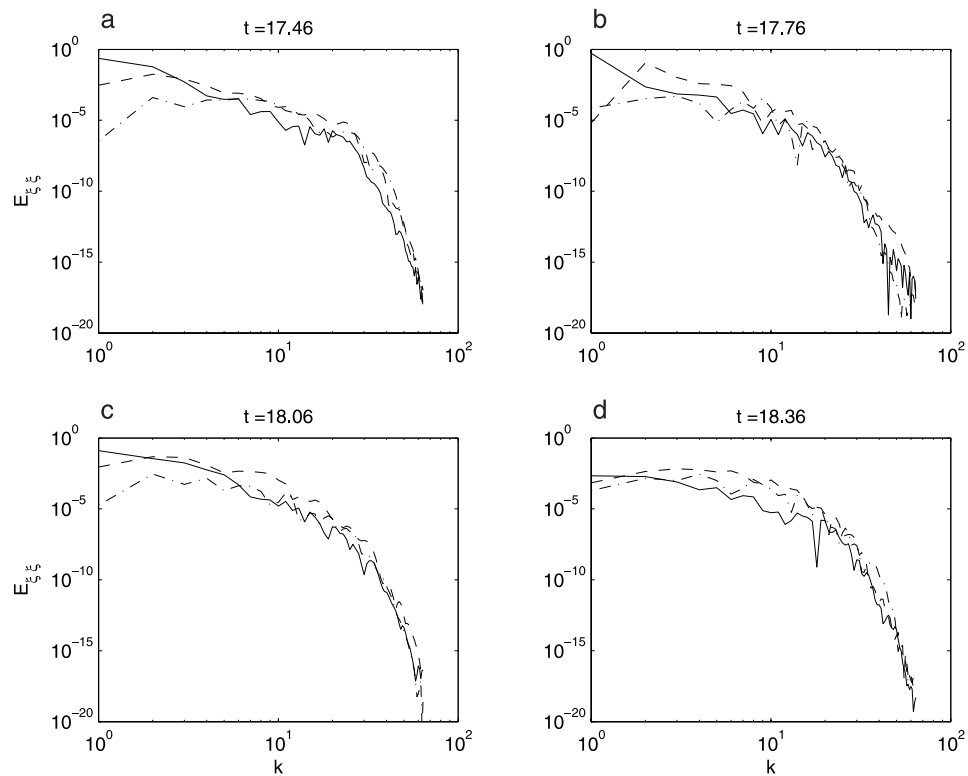


**Figure A2.** Velocity spectra in the  $\xi$ -direction, at times of (a) flow acceleration, (b) maximum onshore flow, (c) flow deceleration, and (d) flow reversal. Solid, dash-dotted, and dashed lines represent spectrum for  $U$ ,  $v$ , and  $W$  velocities in computational space, respectively.

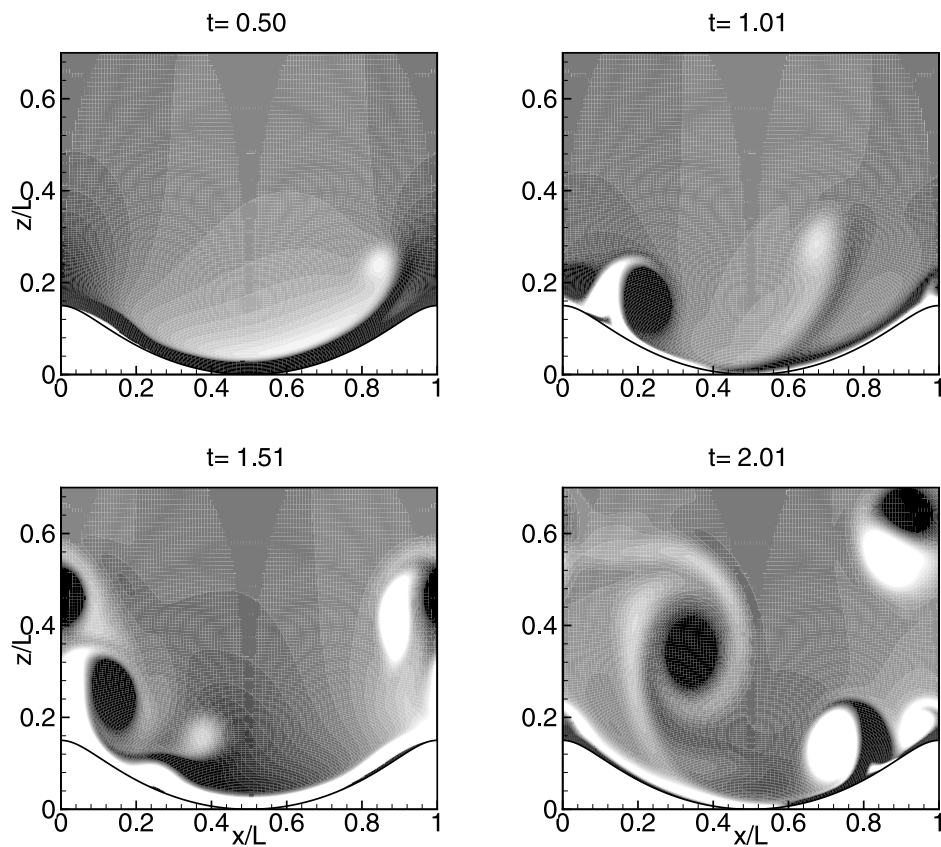


**Figure A3.** Time evolution of vorticity using parameters from *Blondeaux and Vittori [1991] Case 13*,  $R_\delta = 100$ ,  $h/l = 0.15$ , and  $s/l = 0.75$ .

flow, and internal gravity waves) and sample applications (ranging from solitary waves in a tilting tank to flow through a contraction) presented by Winters et al. [2000], results from duplicating a case from Blondeaux and Vittori [1991] are presented in Figure A3. For this case,  $R_\delta = 100$ ,  $h/l = 0.15$ , and  $s/l = 0.75$ . This case represents the highest Reynold number for which detailed data is presented.

[68] Qualitatively, there is good agreement between the two models. The main difference derives from the forcing applied in the model. Blondeaux and Vittori [1991] have use a time-dependent stream function as a forcing mechanism. The elliptic nature of the stream function gives a forcing that more closely follows the ripple shape. Our model uses a forcing based on the horizontal pressure gradient, as would be found under a passing wave. This mechanism causes the initial vortex pair to be shed from the trough, to be followed subsequently by vortex shedding at the ripple crest. Quantitatively, our model also reproduces the bed shear stress as calculated by Blondeaux and Vittori, when accounting for the difference in forcing.

[69] **Acknowledgment.** This work was supported by the Office of Naval Research, under the Shoaling Surface Waves DRI, grant N00014-99-1-0065 and grant N00014-02-1-0486.

## References

- Adams, J. C. (1991), Multigrid software for elliptical partial differential equations: MudPack, technical note, Natl. Cent. for Atmos. Res., Boulder, Colo.
- Ayrton, H. (1910), The origin and growth of ripple mark, *Proc. R. Soc. London, Ser. A*, *84*, 285–310.
- Bagnold, R. A. (1946), Motion of waves in shallow water: Interaction of waves and sand bottoms, *Proc. R. Soc. London, Ser. A*, *187*, 1–15.
- Blondeaux, P., and G. Vittori (1991), Vorticity dynamics in an oscillatory flow over a rippled bed, *J. Fluid Mech.*, *226*, 257–289.
- Calhoun, R. J., and R. L. Street (2001), Turbulent flow over a wavy surface: 1. Neutral case, *J. Geophys. Res.*, *106*(C5), 9277–9293.
- Carstens, M. R., F. M. Neilson, and H. D. Altinbilek (1969), Bedforms generated in the laboratory under oscillatory flow, *Tech. Memo. 28*, Coastal Eng. Res. Cent., Vicksburg, Miss.
- Chang, Y. S., and D. M. Hanes (2004), Suspended sediment and hydrodynamics above mildly sloped long wave ripples, *J. Geophys. Res.*, *109*, C07022, doi:10.1029/2003JC001900.
- Deardorff, J. W., and G. E. Willis (1967), Investigation of turbulent thermal convection between horizontal plates, *J. Fluid Mech.*, *28*, 675–704.
- Fredsoe, J., K. H. Anderson, and B. M. Sumer (1999), Wave plus current over a ripple-covered bed, *Coastal Eng.*, *38*, 177–221.
- Grant, W. D., and O. S. Madsen (1979), Combined wave and current interaction with a rough bottom, *J. Geophys. Res.*, *84*(C4), 1797–1808.
- Hanes, D. M., V. Alymov, and Y. S. Chang (2001), Wave-formed sand ripples at Duck, North Carolina, *J. Geophys. Res.*, *106*(C10), 22,575–22,592.
- Hara, T., and C. C. Mei (1990), Centrifugal instability of an oscillatory flow over periodic ripples, *J. Fluid Mech.*, *217*, 1–32.
- Jonsson, I. G. (1966), Wave boundary layers and friction factors, paper presented at 10th International Conference on Coastal Engineering, Univ. of Tokyo, Tokyo.
- Julien, P. Y. (1998), *Erosion and Sedimentation*, 280 pp., Cambridge Univ. Press, New York.
- Lele, S. K. (1992), Compact finite difference schemes with spectral like resolution, *J. Comput. Phys.*, *103*, 16–42.
- Loftquist, K. E. B. (1986), Drag on naturally rippled beds, *Misc. Pap. CERC-86-13*, Coastal Eng. Res. Cent., Vicksburg, Miss.
- Longuet-Higgins, M. S. (1981), Oscillating flow over steep sand ripples, *J. Fluid Mech.*, *107*, 1–35.
- Mathisen, P. P., and O. S. Madsen (1996a), Waves and currents over a fixed rippled bed: 1. Bottom roughness experienced by waves in the presence and absence of current, *J. Geophys. Res.*, *101*(C7), 16,533–16,542.
- Mathisen, P. P., and O. S. Madsen (1996b), Waves and currents over a fixed rippled bed: 2. Bottom and apparent roughness experienced by currents in the presence of waves, *J. Geophys. Res.*, *101*(C7), 16,543–16,550.
- Mathisen, P. P., and O. S. Madsen (1999), Waves and currents over a fixed rippled bed: 3. Bottom and apparent roughness for spectral waves and currents, *J. Geophys. Res.*, *104*(C8), 18,447–18,461.
- Mei, C. C. (1989), *The Applied Dynamics of Ocean Surface Waves*, *Adv. Ser. Ocean Eng.*, vol. 1., 740 pp., World Sci., River Edge, N. J.
- Nielsen, P. (1992), *Coastal Bottom Boundary Layers and Sediment Transport*, *Adv. Ser. Ocean Eng.*, vol. 4, 324 pp., World Sci., River Edge, N. J.
- Pope, S. B. (2000), *Turbulent Flows*, 771 pp., Cambridge Univ. Press, New York.
- Ralph, M. E. (1986), Oscillatory flows in wavy-walled tubes, *J. Fluid Mech.*, *168*, 515–540.
- Ralph, M. E. (1988), Pressure drop and power dissipation in oscillatory wavy-walled tubes, *J. Fluid Mech.*, *187*, 573–588.
- Ranasoma, K. I. M., and J. F. A. Sleath (1994), Combined oscillatory and steady flow over ripples, *J. Waterway Port Coastal Ocean Eng.*, *120*(4), 331–346.
- Scandura, P., G. Vittori, and P. Blondeaux (2000), Three-dimensional oscillatory flow over steep ripples, *J. Fluid Mech.*, *412*, 335–378.
- Slinn, D. N., and J. J. Riley (1988), A model for the simulation of turbulent boundary layers in an incompressible stratified flow, *J. Comput. Phys.*, *144*, 550–602.
- Sobey, I. J. (1980), On flow through furrowed channels: 1. Calculated flow patterns, *J. Fluid Mech.*, *96*, 1–26.
- Sobey, I. J. (1982), Oscillatory flows at intermediate Strouhal number in asymmetric channels, *J. Fluid Mech.*, *125*, 359–373.
- Sobey, I. J. (1983), The occurrence of separation in oscillatory flow, *J. Fluid Mech.*, *134*, 247–257.
- Toit, C. G., and J. F. A. Sleath (1981), Velocity measurements close to rippled beds in oscillatory flow, *J. Fluid Mech.*, *112*, 71–96.
- Trouw, K., J. J. Williams, and C. P. Rose (2000), Modelling sand resuspension by waves over a rippled bed, *Estuarine Coastal Shelf Sci.*, *50*, 143–151.
- Trowbridge, J. H., and Y. C. Agrawal (1995), Glimpses of a wave boundary layer, *J. Geophys. Res.*, *100*(C10), 20,729–20,743.
- Trowbridge, J. H., and O. S. Madsen (1984), Turbulent wave boundary layers: Model formulation and first order solutions, *J. Geophys. Res.*, *89*(C5), 7989–7997.
- Voropayev, S. I., G. B. McEachern, D. L. Boyer, and H. J. S. Fernando (1999), Dynamics of sand ripples and burial/scouring of cobbles in oscillatory flow, *Appl. Ocean Res.*, *21*, 249–261.
- Wilcox, D. C. (1988), Reassessment of the scale-determining equation for advanced turbulence models, *AIAA J.*, *26*(11), 1299–1310.
- Winters, K. B., H. E. Seim, and T. D. Finnigan (2000), Simulation of non-hydrostatic, density-stratified flow in irregular domains, *Int. J. Numer. Methods Fluids*, *32*, 263–284.

B. C. Barr and D. N. Slinn, Department of Civil and Coastal Engineering, University of Florida, Gainesville, FL 32611-6590, USA. (barr@coastal.ufl.edu; slinn@coastal.ufl.edu)

T. Pierro, Department of Ocean Engineering, Florida Atlantic University, Boca Raton, FL 92093, USA. (tpierro@coastalplanning.net)

K. B. Winters, Scripps Institution of Oceanography, University of California, San Diego, La Jolla, CA USA. (kraig@coast.ucsd.edu)